UNIVERSITÀ
DEGLI STUDI
DI PALERMO

NUOVI CONDUTTORI PROTONICI PER APPLICAZIONI ELETTROCHIMICHE: SINTESI E CORRELAZIONE STRUTTURA - PROPRIETA'

Tesi di Dottorato di:
Dott. Diego Messana

Tutor:
Prof. Antonino Martorana

Coordinatore:
Prof. Michelangelo Gruttadauria

Dottorato di Ricerca in Scienze Chimiche
XXII ciclo
Facoltà di Scienze MM.FF.NN
(Settore scientifico disciplinare: CHIM/03)

2008 - 2010

UNIVERSITÀ
DEGLI STUDI
DI PALERMO

NEW PROTON CONDUCTORS FOR ELECTROCHEMICAL APPLICATIONS: SYNTHESIS AND STRUCTURE – PROPERTIES CORRELATION

Ph.D. Thesis of:
Dott. Diego Messana

Tutor:
Prof. Antonino Martorana

Coordinator:
Prof. Michelangelo Gruttadauria

Dottorato di Ricerca in Scienze Chimiche
XXII ciclo
Facoltà di Scienze MM.FF.NN
(Settore scientifico disciplinare: CHIM/03)

2008 - 2010

"Vincere la materia è comprenderla, e comprendere la materia è necessario per comprendere l'universo e noi stessi"

(Primo Levi)

Contents

1. Solid Oxide Fuel Cells……6

1.1 The operating principle of Fuel Cells……..6

1.2 Types of Fuel Cells……..8

1.3 Efficiency and potential in a Fuel Cell……..10

1.4 Solid Oxide Electrolytes……13

1.5 Electrodes for Solid Oxide Fuel Cells……...17

2. Proton conduction in solid oxides……..19

2.1 Types of solid proton conductors……..19

2.2 Formation of hydroxyl defects in perovskites……...21

2.3 Chemical stability of perovskites……..22

2.4 Mobility of protons in perovskites……22

2.5 Structure of doped perovskites ……24

2.6 Grain boundary conductivity in perovskites……..26

3. New ceramic oxide proton conductors……...28

3.1 The proton conductor Ca:$LaNbO_4$……28

3.2 The proton conductor $LaBaGaO_4$……..31

4. Experimental Techniques……...33

4.1 Thermogravimetric analysis……..33

4.2 X-rays Diffraction and Rietveld analysis……..34

4.3 Synchrotron radiation……36

4.3.1 Synchrotron radiation and X-rays Diffraction……37

4.3.2 X-ray Absorption Fine Structure (XAFS)……..39

4.4 Electrochemical Impedance Spectroscopy……...44

5. Experiments & Results……...47
5.1 Introduction……...47
5.2 Synthesis……47
5.3 TGA Analysis……48
5.4 *In situ* XRD Analysis……50
5.5 EXAFS Analysis……54
5.6 HR-XRD Analysis……61
5.7 EIS Analysis……..64
5.8 Conclusions……70

References……..72

Acknowledgements……75

Curriculum Vitae……78

1. Solid Oxide Fuel Cells

1.1 The operating principle of Fuel Cells

In the last twenty years fuel cells (FC) attracted much interest due to the high efficiency of conversion of chemical into electrical energy and to the low emission of pollutants.

The first fuel cell was constructed by Sir William Grove in 1839: the device, fuelled with pure hydrogen, was operated at room temperature, and a dilute solution of sulfuric acid constituted the electrolyte **[grove1839]**.

The FC operating principle is easy: oxygen is reduced at the cathode and the fuel (hydrogen, hydrocarbon, alcohol, biofuel, etc.) is oxidized at the anode; the electrons travel from anode to cathode through the external circuit providing electrical power, while the ions involved in the cell redox reaction close the electrical circuit traveling through the electrolyte. The state of the art fuel cell technology is based on solid state electrolytes, ensuring reliability and straightforward operation of the device. The reaction products are H_2O and CO_2 when the fuel is a hydrocarbon, but it is only H_2O for hydrogen fuelled devices; the fuel cell reaction also produces heat **(Fig.1.1)** **[steele2001]**. Usually, the anode reaction proceeds with high activation energy, so that a suitable electrical power can be obtained by a large surface area electrode working at high temperature (above 600 °C). At lower operating temperature (about 100°C), a precious metal anode catalyst (usually Pt) is needed. **[larminie,dicks2003]**. If the electrolyte is an anion conductor, the oxide ions produced at the cathode migrate through the electrolyte to the anode where react with fuel. Alternatively, when a proton electrolyte is involved, the protons generated at the anode migrate trough the solid oxide to the cathode where they react with oxygen. The ion conduction is thermally activated and its magnitude varies dramatically, depending on the nature of electrolyte **[haile2003]**.

Hydrogen fuelled FC reactions

Cathode: $\frac{1}{2}O_2 + 2e^- \rightarrow O^{2-}$

Anode: $H_2 \rightarrow 2H^+ + 2e^-$

Electrolyte conduction: O^{2-}

Electrolyte conduction: H^+

Anode: $H_2 + O^{2-} \rightarrow H_2O + 2e^-$

Cathode: $\frac{1}{2}O_2 + 2H^+ + 2e^- \rightarrow H_2O$

[haile2003]

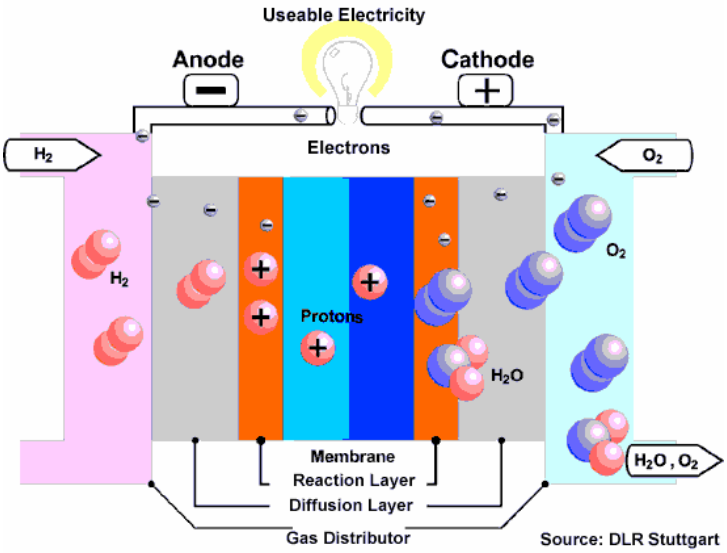

Fig. 1.1. Layout of a proton electrolyte fuel cell. Oxygen is reduced at the cathode and hydrogen is oxidized at the anode: electrons travel to the cathode through the external circuit, while protons diffuse to the cathode through the electrolyte; the reaction product is water **[solarserver]**.

Fuel cells have many advantages compared to conventional power generation systems:

- **"Green energy"**: the fuel cells have very low emissions of pollutants. When the fuel is hydrogen the reaction product is pure water, so achieving the "zero emission" issue. However, it should be noticed that at present the cheapest technology for the production of hydrogen is the steam reforming of natural gases, producing emissions of greenhouse gases.
- **Efficiency**: the fuel cell have high efficiency, in particular FCs working at high temperature can reach an efficiency of 65%.
- **Simplicity**: the essential components of fuel cells are very simple, allowing high reliability.

1.2 Types of Fuel Cells

There are several types of fuel cells, classified according to the exploited electrolyte. A basic list is reported below:

PAFC (Phosphoric acid FC)

PEMFC (Polymer Electrolyte Membrane FC)

MCFC (Molten Carbonate FC)

AFC (Alkali FC)

SOFC (Solid Oxide FC)

Tab. 1.1 gives a synthetic account of the respective characteristics:

	Electrolyte	Ion conducted	Temperature (°C)	Fuel	Efficiency	Power (KW)
PAFC	H_3PO_4	H^+	200	H_2	40%	100[(a)]
PEMFC	Polymer (Nafion)	H^+	70-80	H_2 , CH_3OH	40%	12.5[(b)]
MCFC	Molten carbonate	CO_3^{2-}	650-700	H_2, hydrocarbon, CO	45%	1000[(c)]
AFC	$KOH_{(aq)}$	OH^-	70	H_2	60%	-
SOFC	Solid oxide	O^{2-} or H^+	500-1000	H_2, hydrocarbon, CO	65%	100[(d)]

(a) Allied Signal; **(b)** Fuji Electric; **(c)** MCFC Research Association; **(d)** Siemens Westinghouse.

Tab. 1.1. List of the most important types of fuel cell. Fundamental operation parameters and producer are reported **[yamamoto2000]**, **[steele2001]**, **[haile2003]**.

For the lower temperature fuel cells (PAFC, PEMFC, AFC) a fuel reformer is required; this constitutes a drawback, involving an increase of complexity and a decrease of efficiency. For fuel operation, a Pt anodic catalyst is necessary, that is expensive and irreversibly adsorbs CO at the low working temperatures, so requiring high purity H_2 streams. In contrast, fuel cells operating at high temperature (MCFC and SOFC) allow the straightforward oxidation of both CO and H_2 **[steele2001]**. An important advantage of proton electrolyte fuel cells (PAFC, PEMFC, SOFC) is that the unreacted fuel is not mixed with the reaction products, so allowing straightforward recirculation of unreacted fuel. In **PAFC's** cells the electrolyte is

the phosphoric acid, requiring external reforming and Pt catalyst anode. A severe limitation to the commercialization of this system is the high unit cost. **PEMFC's** utilize a polymeric electrolyte membrane, usually Nafion (a DuPont trade mark), whose high proton conductivity is counterbalanced by the drawbacks of low operating temperature (Nafion decomposes at 120°C). Direct methanol PEMFC's have a very low power. **MCFC's** do not need external reforming and precious metal anode catalyst; however, the nature of the electrolyte, a hot and corrosive mixture of lithium, potassium and sodium carbonates, offsets these advantages.

The **AFC** fuel cells, that utilize the KOH electrolyte, can work only at low temperature so that an expensive Pt catalyst anode and external reforming are required. Another important drawback is the necessity of removal of CO_2 from the cathode. New prospects are given by the **Biological fuel cells**, which try to replicate the way nature derives energy from organic fuels; organic fuels, like methanol or ethanol are used, and electrode reactions are promoted by enzymes. Despite the potential interest, biological fuel cells are still very far from technological maturity **[steele2001]**, **[larminie,dicks2003]**. **SOFCs** use a ceramic solid oxide as electrolyte. The SOFCs have several advantages over other types of fuel cell: the electrolyte is solid, so that the SOFCs do not have the management problems of PAFCs and MCFCs; in particular, they do not need external reforming and expensive anode catalysts; moreover, these devices allow flexibility of employment in a large range of high temperatures, easy handling of the excess heat for auxiliary energy production, use of cheaper materials. In contrast, the SOFCs utilize relatively weak and brittle structural component **[yamamoto2000]**. Among solid oxide anionic conductors, the most utilized is yttria-stabilized zirconia, while solid oxide proton conductors are to date affected by unresolved problems concerning low grain boundary conductivity or low chemical stability **[kreuer2003]**.

Due to the higher efficiency and greater fuel flexibility, high temperature SOFC's are generally preferred for stationary applications. For portable devices, low temperature fuel cells are favored, in particular PEMFC's, because they have a rapid start-up and minimize the thermal stresses of materials **(Fig.1.2)** **[haile2003], [larminie,dicks2003]**.

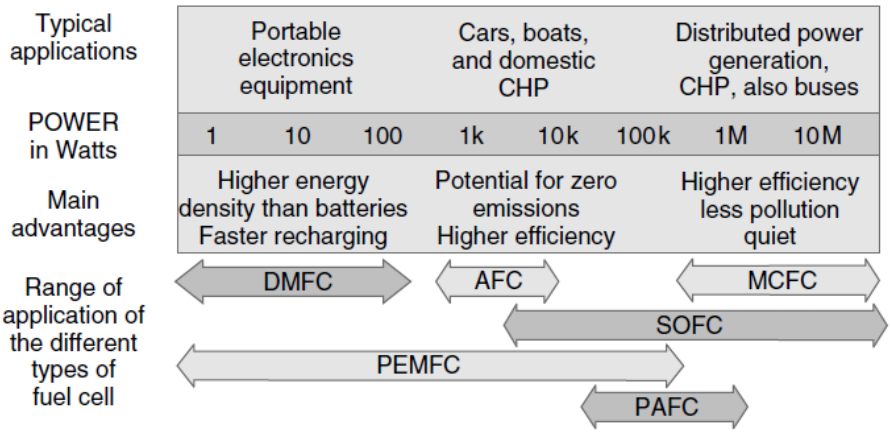

Fig. 1.2. Chart summarizing the applications and advantages of different types of fuel cells **[larminie,dicks2003].**

.

1.3 Efficiency and potential in a Fuel Cell

If an electrochemical system performs a reversible transformation, the electrical work is equal to the variation of the Gibbs free energy. Therefore, the electromotive force (or reversible open circuit voltage) of a hydrogen-fuelled cell is:

(1.01) $$E_{ocv} = -\frac{\Delta G}{2nF}$$

where ΔG is the change of Gibbs free energy, F is the Faraday constant, n is the number of moles of fuel and the factor *2* accounts for the number of electrons involved in the redox reaction $H_2 + \frac{1}{2}O_2 \rightarrow H_2O$

The Gibbs free energy of the reaction is:

(1.02) $$\Delta G = \Delta G^0 - RT \ln\left(\frac{P_{H2} \cdot P_{O2}^{1/2}}{P_{H2O}}\right)$$

Where ΔG^0 refers to the standard states of all species **[larminie,dicks2003], [haile2003]**.

The limit value of efficiency is the **Gibbs efficiency (η_G)**:

(1.03) $$\eta_G = \frac{\Delta G}{\Delta H} = -\frac{2nFE_{ocv}}{\Delta H}$$

Where ΔH is the heat of the reaction.

In **Tab. 1.2**, the molar Gibbs free energies (Δg) for some useful temperatures, the corresponding maximum value of open circuit voltage (E_{ocv}) and the maximum efficiency, or Gibbs efficiency (η_G) when the fuel is hydrogen are reported. **[larminie,dicks2003]**

T (°C)	Δg (KJ/mol)	E_{ovc} (V)	η_G
25	-273.2	1.23	83%
80	-228.2	1.18	80%
200	-220.4	1.14	77%
600	-199.6	1.04	70%
800	-188.6	0.98	66%

Tab. 1.2. For selected working temperatures of hydrogen fuelled cells, the molar Gibbs free energy (Δg), the corresponding maximum value of open circuit voltage (E_{ovc}) and the Gibbs efficiency (η_G) are reported **[larminie,dicks2003].**

The **open circuit voltage** can be calculated by Nernst equation:

(1.04) $$E_{ocv} = E^0 + \frac{RT}{2F}\ln\left(\frac{P_{H2}\cdot P_{O2}^{1/2}}{P_{H2O}}\right)$$

However, when a fuel cell is put to use, the measured voltage is considerably less than open circuit voltage, especially at high temperatures. The **Fig. 1.3** shows the performance of a SOFC operating at about 800°C. **[larminie,dicks2003]**

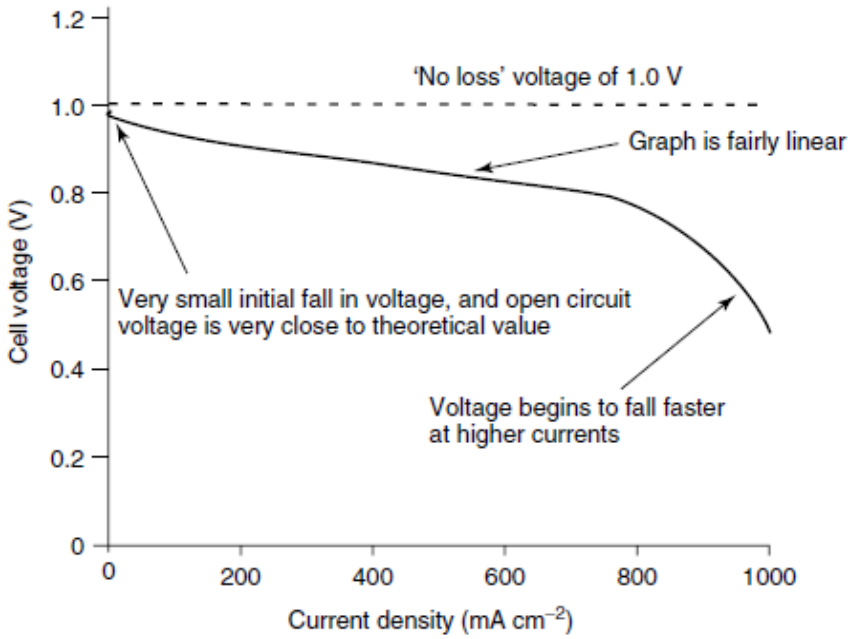

Fig. 1.3. Cell voltage vs. current density of a typical SOFC operating at about 800°C. **[larminie,dicks2003]**.

The **potential of a fuel cell** is given by the value of open circuit voltage minus all sources of losses: the activation overvoltage (ΔV_{act}), the ohmic losses (ΔV_{ohm}) and the concentration losses (ΔV_{diff})

(1.05) $$V_{fuelcell} = E_{ocv} - \Delta V_{act} - \Delta V_{ohm} - \Delta V_{diff}$$

Where: E_{ocv} is given by **eq. 1.04**, and the after terms of the right member of **eq. 1.05** are defined by the **eq.s 1.06-1.08** below reported. **[larminie,dicks2003], [haile2003]**.

The **activation overvoltage** at the surface of an electrode is given by the Tafel empirical equation:

(1.06) $$\Delta V_{act} = \frac{RT}{2\alpha F}\ln\left(\frac{i + i_n}{i_0}\right)$$

where α is the charge transfer coefficient and depends on reaction of electrode and on its material manufacturing; i is the current density, i_n is the internal current density (a little quantity of electrons that migrate through the electrolyte and not trough the current collectors), and i_0 is the **exchange current density**. When the circuit is open, at zero current density (i), is not true that there are any activities at the electrodes: the cell reaction is at dynamic equilibrium, so there is a flow of electrons from and to the electrolyte, it is the exchange current density (i_0). If the exchange current density is high then the surface of electrode is more active. This current density is crucial in controlling the performances of a fuel cell, its value have to be higher as possible. Generally, in a fuel cell the overvoltage at the anode is negligible compared to that of the cathode. To decrease the overvoltage, use of catalysts, improvement of electrode surface area and increase of working temperature are needed. A loss of potential is also due to some amount of fuel that diffuses to cathode through the electrolyte (**fuel crossover**).

The **Ohmic losses** (**eq.1.07**), due to power dissipate by all resistance, can be decreased using electrodes as thin as possible and with higher conductivity is possible.

(1.07) $$\Delta V_{ohm} = i \cdot R$$

The resistance R includes terms of electrolyte, electrodes and current collectors.

When the reagent gas moves into the electrode the pressure is decreasing while the gas is reacted, this reduction in pressure depends on the electric current of the cell and will give a reduction in voltage. In **equation 1.08** we see that the change in voltage, **concentration losses**, is given by the change in pressure of gas at each electrode:

(1.08) $$\Delta V_{diff} = \frac{RT}{2F}\ln\left(\frac{P_1}{P_2}\right) = \frac{RT}{2F}\ln\left(1 - \frac{i}{i_1}\right)$$

where i_1 is a limiting current density at which the fuel is used up at a rate equal to its maximum supply speed. Another approach uses an empirical equation and gives better fit to the results:

(1.09) $\Delta V_{diff} = m\exp(ni)$

where m will typically be about $1*10^{-4}$V, and n about $8*10^{-3}$cm^{2}mA^{-1} in a SOFC **[larminie,dicks2003]**.

The total **efficiency η of fuel cell** can be calculated by:

(1.10) $\eta = \eta_G \eta_V \alpha$

where α is the fraction of fuel used**,** η_G is the Gibbs efficiency **(eq.1.03)** and η_V is the voltage efficiency:

(1.11) $\eta_V = \frac{E}{E_{ocv}}$

where E is the voltage at closed circuit while E_{ocv} is the open circuit voltage **[steele2001]**.

1.4 Solid Oxide Electrolytes

The anion conductivity of certain solid oxide ceramics have known since more than hundred years. **In 1899 Nernst** first discovered that Y_2O_3-doped ZrO_2 was a solid oxide ion conductor **[nernst1899].** The substitution of Zr^{4+} with Y^{3+} involves the formation of oxygen **vacancies** for charge compensation. The defect reaction can be written in Kröger-Vink notation as:

(1.12) $Y_2O_3 \rightarrow 2Y'_{Zr} + V_o^{\bullet\bullet} + 3O_O^{\ x}$

The conductivity is due to these oxygen vacancies:

(1.13) $\sigma = e\mu[V_O^{\bullet\bullet}]$

where e is the effective charge, μ is the mobility of vacancies and $[V_0]$ their concentration **[yamamoto2000]**.

An **ideal electrolyte** has to fulfill further requirements:

- High oxygen ion, or proton, conductivity
- Low electronic conductivity, to minimize the internal current
- Chemical stability under reducing, oxidizing condition and in presence of CO_2.
- Impermeability at fuel and air
- Easy fabrication of dense thin film
- Mechanical integrity at operating temperatures. **[haile2003], [yamamoto2000]**.

Fig. 1.4 shows specific conductivity for selected solid-oxide electrolytes versus reciprocal temperature.

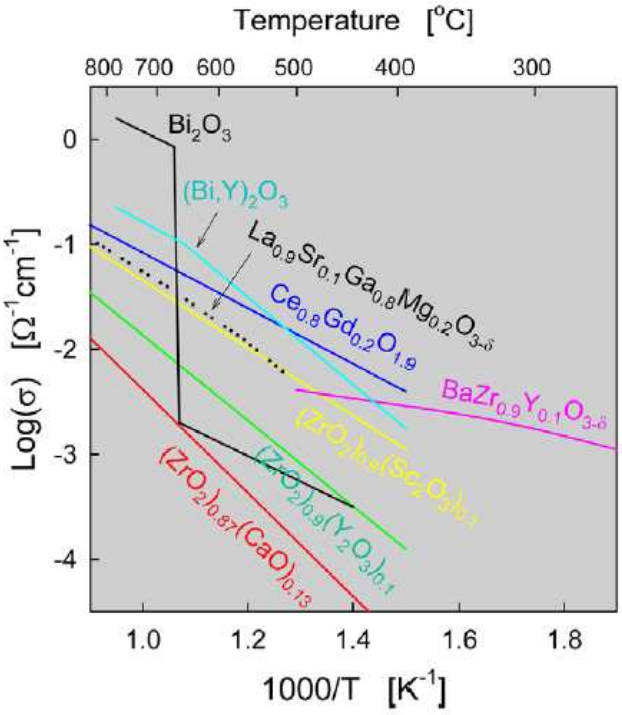

Fig. 1.4. Specific conductivity for selected solid-oxide electrolytes versus reciprocal temperature **[haile2003]**.

The classical oxygen ion conductor is the stabilized ZrO_2, which has a fluorite structure. The dopant Sc_2O_3 gives the highest conductivity. Despite its high conductivity, **$(ZrO_2)_{1-x}(Sc_2O_3)_x$ (SSZ)** is not the most used electrolyte in fuel cell technology, because it is expensive and hardly stable at high temperatures. The typical dopant of zirconia is Y_2O_3: the highest conductivity (0.14 Scm^{-1} at 1000°C) of yttria stabilized zirconia **(YSZ)** is reached in correspondence of the composition **$(ZrO_2)_{0.8}(Y_2O_3)_{0.2}$**. YSZ has been widely used, due to a relatively high anion conductivity, a low electronic conductivity and good stability under reducing and oxidizing atmosphere **[yamamoto2000], [arachi1999].**

The major drawback of YSZ is represented by the very high working temperature; the most investigated oxide for the production of electrolyte working at lower temperature is CeO_2, with fluorite structure. In this case Sm and Gd are the dopants that give the highest values of conductivity. The conductivity of **$Ce_{0.8}Gd_{0.2}O_{1.9}$ (GDC)** is 1.2* 10^{-2} Scm^{-1} at 800°C and 3.7*10^{-3} Scm^{-1} at 600°C. At the same temperature and dopant concentration, the ionic conductivity of ceria is about one order of magnitude greater than zirconia, because the larger ionic radius of Ce^{4+} wrt Zr^{4+} produces a more open structure through which anions can migrate. Despite the better ion mobility, GDC cannot be used beyond ≈800 °C because at

higher temperatures and in reducing condition Ce^{4+} can be reduced to Ce^{3+}, involving a high electronic conductivity that increases with a $P_{(O2)}^{-1/4}$ dependence. **[haile2003], [tuller1979].** A lot of oxides with perovskite structure, in a large variety and concentration of dopants show oxide ion conduction and are diffusely studied. For examples **$BaTh_{0.9}Gd_{0.1}O_3$ (BTG)** was used as electrolyte with a thickness of 0.13cm at 550°C; its anion conductivity was estimated to be $8.7*10^{-2}$ Scm^{-1} **[yamamoto2000], [cook1992]**. **$La_{0.9}Sr_{0.1}Ga_{0.8}Mg_{0.2}O_{2.85}$ (LSGM)** has an anion conductivity of more then 0.1 Scm^{-1} at 800°C and a good chemical stability, but secondary phases are often detected in the grain boundary (GB) that increase the GB resistivity. A further drawback of LSGM is that it reacts with Ni, a typical material for anode, to form $LaNiO_3$ **[yamamoto2000], [ishiara1994]**.

One outstanding objective of the research about fuel cells is the development of solid oxide proton conductors. To obtain proton conduction, proton defects are introduced into the oxide by dissociative incorporation of water that, as can be easily recognized from the relevant defect reaction,

(1.14) $H_2O_{(g)} + V_O^{\bullet\bullet} + O_O^{\ x} \Leftrightarrow 2OH_O^{\bullet}$

requires the presence of reticular oxygen vacancies, usually created by insertion of lower valence cationic dopants.

From **eq. 1.14**, the capacity of the solid oxide to incorporate protons depends on its Broensted basicity and therefore the formation of proton defects is not compatible with a high stability of the oxide against reaction with acidic species such as CO_2 and SO_2 **[kreuer2003].**

In **fig. 1.5** the proton conductivities of some proton conductor electrolytes *vs.* reciprocal temperature are reported, and in **fig. 1.6** the water incorporation and decomposition by CO_2 equilibrium constants are compared for selected proton conductors.

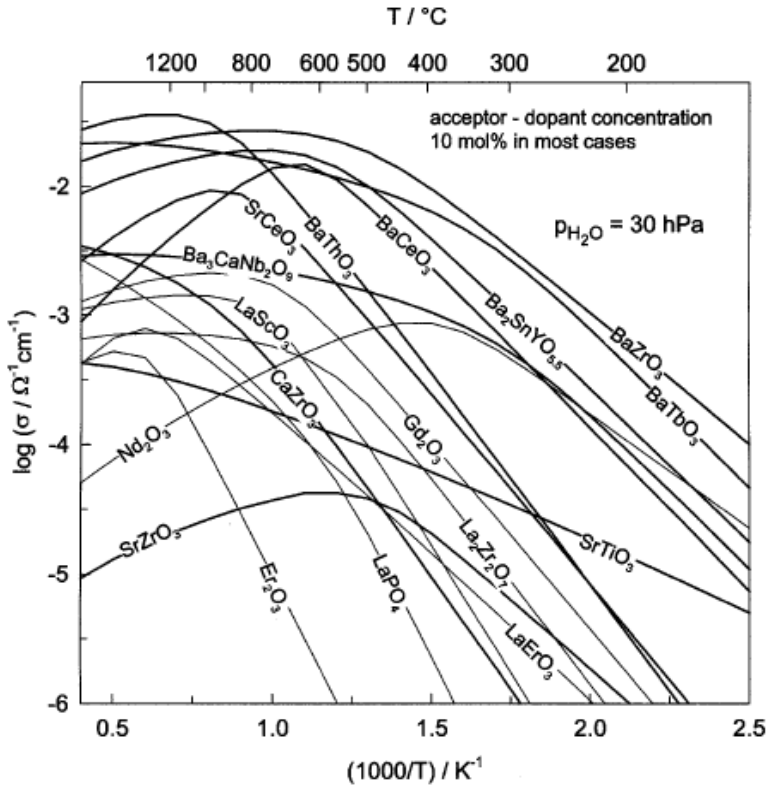

Fig. 1.5. Specific conductivity for some proton conductor electrolytes versus reciprocal temperature at a partial pressure of water of 30 hPa **[kreuer2003]**.

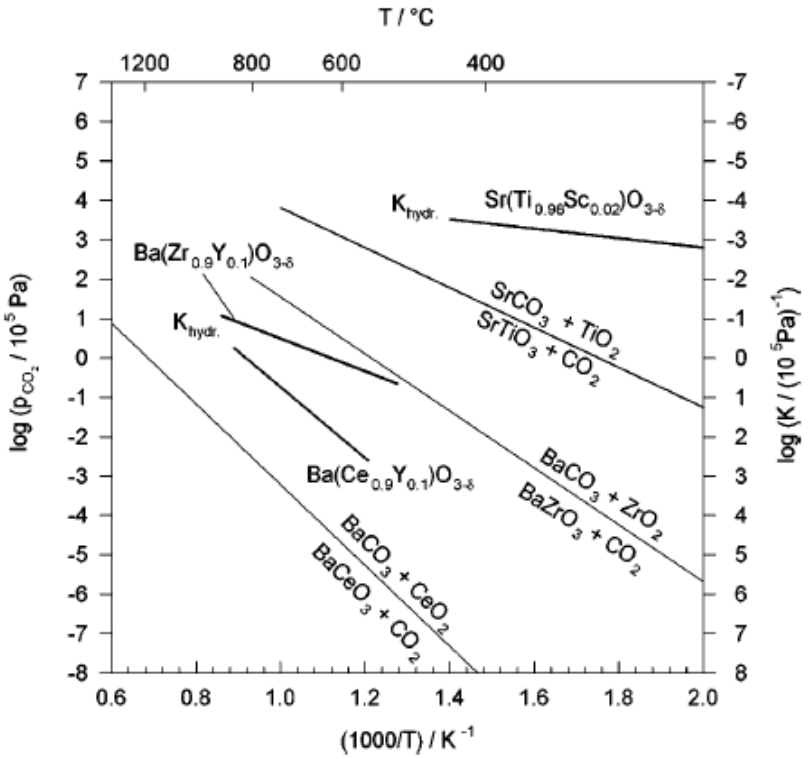

Fig. 1.6. Equilibrium constants of water incorporation and of decomposition by CO_2 for selected proton conductors **[kreuer2003]**.

Some of the best proton conductors have a perovskite-type structure, such as the $BaCeO_3$-based oxides**,** which have high proton conduction and high constant of hydration. An important drawback is that these materials have poor chemical stability against CO_2. The proton conductivity of **$BaCe_{0.9}Sm_{0.1}O_{2.95}$ (BCS)** is about 10^{-2} $\Omega^{-1}cm^{-1}$ at 500°C. **[kreuer2003], [iwahara1988]**. Also $BaZrO_3$-based materials have a perovskite structure. The bulk conductivity of **$BaZr_{0.8}Y_{0.2}O_{2.9}$ (BZY)** is slightly higher than $BaCeO_3$-based oxides and at the present this is the only material that combines high bulk proton conductivity with high chemical stability. The major disadvantage of BZY is the high resistivity of grain boundary that limits its use for fuel cell application **[kreuer2003], [katahira2000]**.

1.5 Electrodes for Solid Oxide Fuel Cells

The demands of fuel cell electrodes are extreme and the research in this field is very active. An **ideal electrode** has to fulfill several requirements:

- High electronic conductivity
- Transport of gas and ionic species
- Porosity and high surface areas to enhance the maximum interaction between the reagents
- Chemical compatibility with the electrolyte
- Mechanical compatibility with the electrolyte at operating temperatures.

At present the most used cell is **Ni-YSZ|YSZ|LSM** made by **Siemens-Westinghouse.** In this cell the anode material is a Ni / $(ZrO_2)_{1-x}(Y_2O_3)_x$ cermet, and the cathode composition is $La_{1-x}Sr_xMnO_{3-\delta}$ (x = 0.15 – 0.25); the porosities of electrodes are typically 25-40 vol%. After deposition of $La(Sr)CrO_3$ interconnections, the thick-film (30-40μm) is made by electrochemical vapor deposition (EVD). The anode is prepared from a NiO and YSZ mixture which is subsequently reduced in situ. This system ensures an efficiency of 60%. A tubular 100kW system fabricated by Siemens-Westinghouse has efficiently worked for over 20,000 hrs **[steele2001], [haile2003].** Recently LSM cathode was changed with a composite YSZ:LSM = 50:50. This change has given an increase in peak power densities, for laboratory cell operated on hydrogen, from about 250mWcm^{-2} at 1000°C to 2 Wcm^{-2} at 800°C **[haile2003], [singhal2002]**.

For each electrolyte, suitable electrodic materials must be selected: for instance, good performances are described for **Ni-YSZ|GDC|LSFC** cell (LSFC=$La_{0.8}Sr_{0.2}Fe_{0.8}Co_{0.2}O_3$) **[yamamoto2000], [van berkel1995]** and for **Ni|LSGM|SSC** (SSC=$Sm_{0.5}Sr_{0.5}CoO_3$) **[yamamoto2000], [ishiara1998]**.

As concerns proton conducting SOFCs, some experiments were simply focused on proof of principle utilizing Pt for both electrodes. Kreuer reports that a pellet 15Y:$Ba(Zr_{0.9}Ce_{0.1})O_{3-\delta}$ was covered with a Pt paste as electrodes **(Pt|B(ZC)Y|Pt)** . The maximum power was 30mWcm^{-2} at 800°C, a value lower than the expected value due to grain boundary impedance and significant electrodes polarization **[kreuer2003]**.
A cell was made using the proton conductor $BaCe_{0.9}Sm_{0.1}O_{3-\delta}$ and with a porous Ni anode and $La_{0.6}Ba_{0.4}CoO_3$ cathode. The maximum short-circuit current density of **Ni|BCS|LBC** cell was 900mAcm^2 at 1273°C but proton conduction was predominant below 1000°C **[haile2003], [iwahara1993]**.

In **Tab.1.3** are summarized the selected cells and their characteristics.

SOFC	Type of conduction	Characteristics	References
Ni-YSZ|YSZ|LSM	O^{2-}	efficiency 60%. a tubular system has worked at 100kW for over 20.000 hrs	**[steele2001]**
Ni-YSZ|YSZ|YSZ:LSM	O^{2-}	from about 250mWcm^{-2} at 1000°C to 2 Wcm^{-2} at 800°C	**[singhal2002]**
Ni-YSZ|GDC|LSFC	O^{2-}	a cell voltage of 0.7V was obtained at 150mAcm^{-2} and 603°C	**[van berkel1995]**
Ni|LSGM|SSC	O^{2-}	a cell voltage of 0.7V was obtained at 500 mAcm^{-2} and 600°C	**[ishiara1998]**
Pt|B(ZC)Y|Pt	H^+	maximum power was 30mWcm^{-2} at 800°C	**[kreuer2003]**
Ni|BCS|LBC	H^+	maximum current density was 900mAcm^2 at 1273°C	**[iwahara1993]**

Tab. 1.3. Are reported some selected SOFCs and their characteristics.

2. Proton conduction in solid oxides

2.1 Types of solid proton conductors

Many different types of solids show proton conduction; in particular, the state-of-the-art ceramic solid oxides have a maximum conductivity of about 10^{-2} - 10^{-3} S cm^{-1}. Generally, proton conductivity increases until a given temperature is reached, and then decreases due to decomposition and/or water loss.

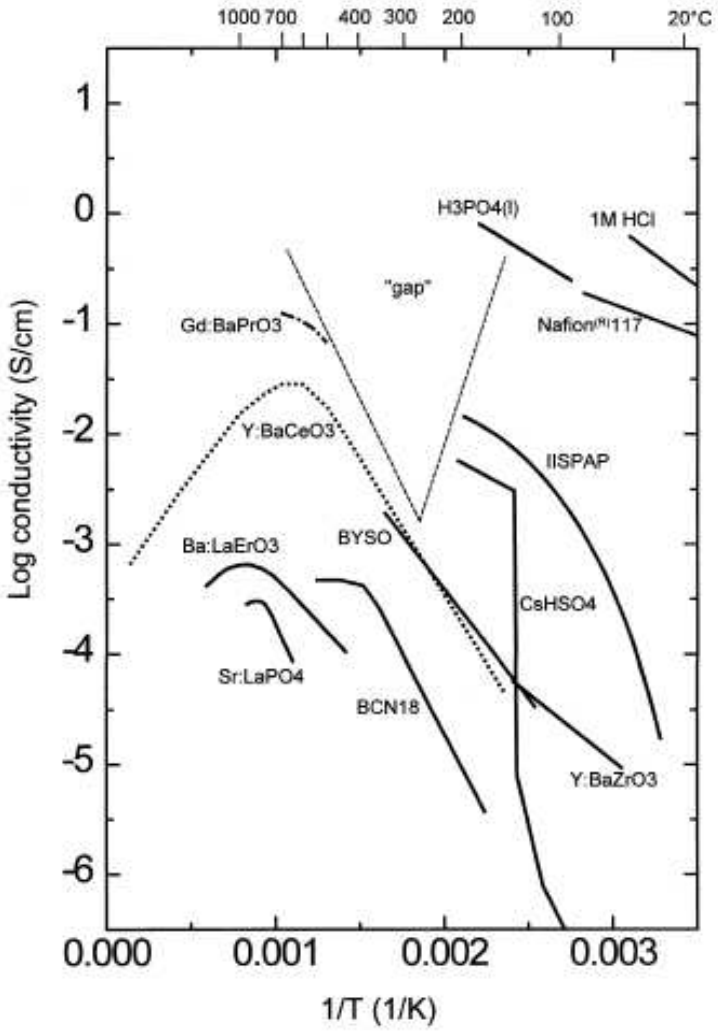

Fig. 2.1. Selected literature data of different types of proton conductor solid materials. The polymer Nafion has the best proton conduction, but it decomposes at 120°C. $CsHSO_4$ becomes a fast proton conductor at about 140°C, but it melts at 200°C. The $BaCeO_3$-based oxides have high proton conduction and high constant of hydration, but they have poor chemical stability against CO_2. The $BaZrO_3$-based oxides have high bulk conductivity and high chemical stability but they have high resistivity of grain boundary **[norby1999]**.

A brief account of the most investigated solid state proton conductors includes:

- **Hydrated polymer membranes**. These materials enclose water pools where a liquid-like mechanism of proton transport takes place. The protons are often introduced by ion exchange of alkali cations. The best proton conductor in this class of solids is **Nafion** (a DuPont trade mark), that has proton conduction comparable to liquid H_3PO_4. The working temperature of Nafion in fuel cells is less than 120° C, because at higher temperatures the polymer decomposes **[norby1999]**.
- **Organic and inorganic hydrates.** The conduction mechanism takes place with the formation of defects such as proton vacancies or interstitials, which can be formed by thermal intrinsic disorder or aliovalent doping. A typical material of this class is **$CsHSO_4$**, which becomes a fast proton conductor at about 140°C, and has an upper working temperature of about 200°C, in correspondence to the $CsHSO_4$ melting temperature. **[norby1999]**
- **Ceramic solid oxides.** Protons are inserted in the structure by dissociative incorporation of hydrogen **(eq. 2.01)** or water **(eq. 2.02)**. In Kröger-Vink notation:

  (2.01) $H_{2(g)} + 2O_O^{\,x} \Leftrightarrow 2OH_O^{\bullet} + 2e^-$

  (2.02) $H_2O_{(g)} + V_O^{\bullet\bullet} + O_O^{\,x} \Leftrightarrow 2OH_O^{\bullet}$

  When hydrogen is fed, **eq. 2.01**, formation of delocalized electrons takes place, while dissociative incorporation of water, **eq. 2.02**, needs oxygen ion vacancies to host hydroxyl ions. The highest conductivity of this class is achieved by **perovskite-like oxides**. In particular, $BaCeO_3$-based oxides have high proton conduction and high hydration constant, but poor chemical stability towards CO_2. On the other hand, $BaZrO_3$-based oxides have high bulk conductivity and high chemical stability, but are affected by high grain boundary resistivity. **[norby2004], [kreuer2003]**.

The first that discovered and treated hydrogen defects in oxides was Carl Wagner in 1960. The scientific interest in solid oxide proton conductors was strongly enhanced when **Iwahara et al., in 1980's,** showed that certain perovskites have high proton conductivity at elevate temperatures and demonstrated many possible applications **[iwahara1981]**.

2.2 Formation of hydroxyl defects in perovskites

When a doped perovskite, with general stoichiometric formula $A(B_{1-x}D_x)O_{3-\delta}$, is in equilibrium with water vapor, proton defects are formed according to **eq. 2.02**; the hydration equilibrium constant is given by:

(2.03) $$K = \frac{[OH_O^{\bullet}]^2}{[V_O^{\bullet\bullet}][O_O^{x}]P_{H2O}}$$

Taking into account the electroneutrality condition **(eq. 2.04),** where [D'] represents the trivalent dopant concentration, and the stoichiometric balance **(eq 2.05)**, it is possible to calculate the concentration of proton defects **(eq. 2.06)**:

(2.04) $$2[V_O^{\bullet\bullet}] + [OH_O^{\bullet}] = [D']$$

(2.05) $$[O_O^{x}] + [V_O^{\bullet\bullet}] + [OH_O^{\bullet}] = [O] = 3$$

(2.06) $$[OH_O^{\bullet}] = \frac{[O]KP_{H2O}\left(1 - \sqrt{\frac{2[D']}{[O]} + \frac{[D']^2}{[O]^2} + \frac{8[D']}{[O]KP_{H2O}} - \frac{4[D']^2}{[O]^2 KP_{H2O}}}\right)}{4 - KP_{H2O}}$$

At low P_{H2O} the dopant is compensated by oxygen vacancies, while at high P_{H2O} the dopant is compensated by hydroxyl defects.**[norby2004], [kreuer2003]**

As the dissociative incorporation of water is accompanied by a weight increase, the concentration of proton defects can be experimentally determined by thermogravimetric analysis (**TGA**) as a function of temperature or of water-partial pressure. Since K(T) generally shows an Arrhenius behavior, the enthalpy and entropy of hydration may also be obtained:

(2.07) $$\ln K = T\Delta S^0 - \Delta H^0$$

[kreuer1999], [giannici2007a].

For cubic perovskites, having only one kind of oxygen site, the fit of eq. **2.06** to the experimental hydration isobars is good, and is very good also for perovskites that have a slight orthorhombic distortion, then presenting two kinds of oxygen sites (for example Y:$BaCeO_3$). Only for perovskites that have a high deviation from ideal cubic structure, like for example Y:$SrZrO_3$, the hydration isobars can not be fitted by the **2.06** expression. In particular, the existence of different oxygen sites reduces the saturation limit **[kreuer1999], [kreuer2003]**.

The hydroxyl defects formation **(2.02)** may be considered an amphoteric reaction because a water proton is transferred to a lattice oxygen and the hydroxyl ion fills an oxide vacancy. The hydration enthalpy in perovskites becomes more negative in the order: titanates >

zirconates > cerates; Kreuer et al. suggest that this behavior is indicative that the basicity is a crucial parameter that controls the formation of hydroxyl defects **[kreuer1999], [kreuer2003]**. Norby et al. show that there is a correlation between the hydration enthalpy and the difference $\Delta\chi_{B\text{-}A}$ in electronegativity between the cations populating the B-site and the A-site; perovskites with small $\Delta\chi_{B\text{-}A}$ have the more negative hydration enthalpy **[norby2004]**.

The low hydration entropy of Y:$BaZrO_3$ can explain the stabilization of hydroxyl defects up to quite high temperature, despite the relatively low hydration enthalpy **[kreuer1999]**. Giannici et al. have showed that hydration entropy is correlated with the structure of perovskites: In:$BaCeO_3$ has very regular InO_6 octahedra and hydration entropy less than Y:$BaCeO_3$, in which the YO_6 octahedra are distorted **[giannici2007a]**.

2.3 Chemical stability of perovskites

The fact that the capacity of solid oxide to incorporate water depends also on its Broensted basicity suggests that the formation of proton defects is not compatible with a high stability of the oxide towards reaction with acidic species such as CO_2 and SO_2 that involves a decomposition of ceramic oxide (for example reaction **2.08**).

(2.08) $BaCeO_3 + CO_2 \leftrightarrow BaCO_3 + CeO_2$

Indeed, the chemical stability of perovskites increases with the decrease of the stability of hydroxyl defects, in the order: titanates > zirconates > cerates **(Fig. 1.6)** **[kreuer2003]**.

The stability of $SrCeO_3$, showing a strong orthorhombic distortion, is almost equal to that of $BaCeO_3$. Therefore, the chemical stability of perovskites versus acid species is affected to a minor extent by the reduction of symmetry. The chemical stability of $BaZrO_3$ is higher than $BaCeO_3$, due to the higher covalency of the Zr-O bond **[kreuer2003]**.

2.4 Mobility of protons in perovskites

In a hydrated perovskite the free energy decrease due to O-H bond formation is competing with the free energy increase involved in the consequent lattice distortion caused by hydrogen bond establishment between neighboring oxygens. **Quantum MD-simulations** demonstrate that in $BaCeO_3$–based materials these free-energy contributions are balanced for a wide range of oxygen separation (250-300 pm). **[kreuer2003], [kreuer2000]**. The strong red-shifted OH-stretching absorption observed by infrared spectroscopy (**IR**) demonstrates the formation of strong hydrogen bonds. Instantaneous configurations like the one depicted

in **Fig. 2.2b**, promoted by lattice thermal vibration, are possible and allow proton hopping to eight neighboring oxygen sites. **[kreuer2003], [kreuer2000]**.

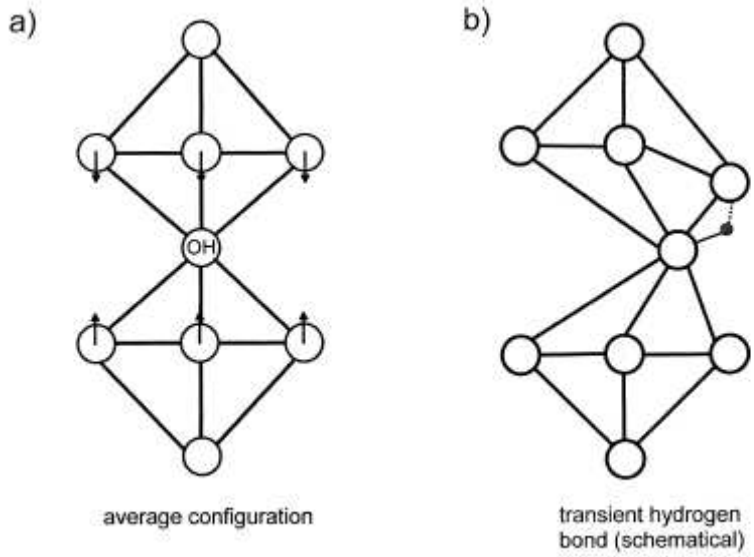

Fig. 2.2. Hydrogen bond in $BaCeO_3$: a) average configuration, b) instant configuration allowing proton hopping **[kreuer2000]**.

When the configuration of O-H···O is linear, the calculated activation enthalpy for proton hopping in cubic perovskites is 0.15 eV; however, the observed value is noticeably higher (about 0.4-0.6 eV), probably because the repulsive interaction between the proton and the highly charged B-site cation prevents the formation of linear O-H···O configuration. Actually, this interpretation can be supported by the higher activation enthalpies observed when the B-site is doped with pentavalent species **[kreuer2003], [kreuer2000]**.

A symmetry decrease has tremendous effect in the mobility of protons. $Y:SrCeO_3$ is less symmetric than $Y:BaCeO_3$, its large orthorhombic distortion giving rise to two nonequivalent oxygen sites and therefore to two different chemical environments. As a consequence, the non-homogeneity of proton reorientation freedom throughout the solid oxide produces an average increase of activation energy. **[kreuer1999], [kreuer2003]**.

The mobility of proton is also sensitive to chemical perturbation induced by the dopant. In $Y:BaCeO_3$ the proton mobility decreases as a function of the dopant concentration: the introduction of Y increases the basicity of oxygens, and therefore involves the formation of stronger O-H bonds **[kreuer1999], [kreuer2003]**.

2.5 Structure of doped perovskites

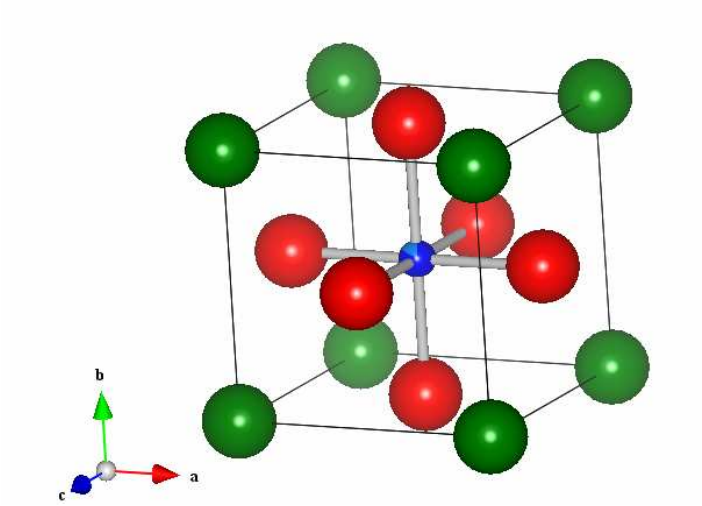

Fig. 2.3. Structure of perovskiteY:$BaZrO_3$. The smaller Zr^{4+} cation (deep blue balls) resides in the center of corner –sharing ZrO_6 octahedra (O^{2-} are the red balls). The larger Ba^{2+} cations (green balls) are located in the vertices of the cubic cell.

In a perovskite ABO_3 **(Fig. 2.3)**, the smaller B-cation resides in the center of corner-sharing BO_6 octahedra. The larger A-cation is located in the cavities between the octahedra and is coordinated by twelve oxygens. An ideal perovskite is cubic but in the case of $BaCeO_3$ or $SrCeO_3$ an orthorhombic distortion takes place **[giannici2007a]**.

Mobility and stability of hydroxyl defects are strongly influenced by the structure of the perovskite, **so that it is very important to study the long range and the local structure of a solid proton conductor to understand and to improve its properties.** Giannici et al. recently studied the $BaCeO_3$ perovskite doped with three different trivalent cations: the long-range structure was investigated by X-ray diffraction **(XRD)** and the local structure by X-ray absorption spectroscopy **(EXAFS) (Fig. 2.4) [giannici2007a], [giannici2007b], [giannici2010].**

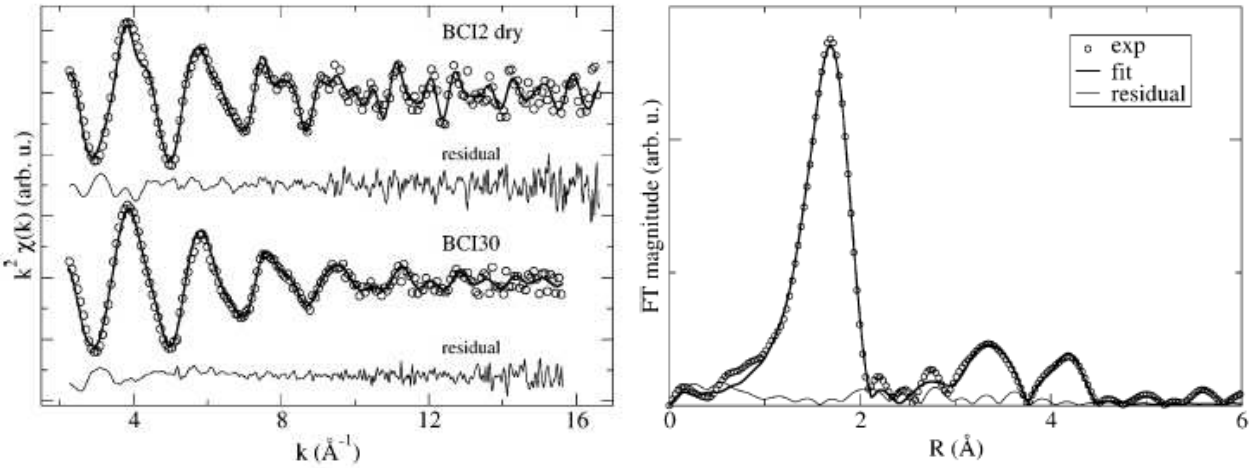

Fig. 2.4. The left frame shows the experimental EXAFS spectra (at -193°C) and the best fit for In:$BaCeO_3$ doped at 2% and 30%. The right frame reports the Fourier transform and the best fit for the 30% In-doped sample **[giannici2007a]**.

The three dopants of barium cerate, In^{3+}, Y^{3+} and Gd^{3+} respectively, have ionic radius smaller, nearly equal and larger than Ce^{4+}. Despite the very small ionic radius mismatch between Ce^{4+} and Y^{3+}, the YO_6 octahedra are axially distorted and the hydroxyl defects preferentially interact with the doped B-sites. EXAFS analysis demonstrated that yttrium solubility in barium cerate is limited to about 17% of the available B sites. Also for Gd:$BaCeO_3$ the dopant solubility does not exceeds about 20% and the proton defects are preferentially localized around the doped B-sites. GdO_6 octahedra are quite strained and the second coordination Gd-Ba distances are very contracted. Both "good" dopant Y^{3+} and Gd^{3+} induce a strong and localized perturbation of local structure. On the contrary, the insertion in barium cerate of indium is possible in the whole compositional range. The InO_6 octahedra are always regular and the hydroxyl defects do not interact with a preferential B-site. In^{3+} is able to effectively release the structural strain over the surrounding lattice, allowing complete dopant solubility. On the other hand, proton diffusivity in In:$BaCeO_3$ is definitely lower than in the other two compounds **[giannici2007a], [giannici2010]**.

2.6 Grain boundary conductivity in perovskites

The **grain boundary** is the interface between two crystalline grains in a polycrystalline material as shown by the reported **SEM** (scanning electron microscope) images **(Fig 2.5)**.

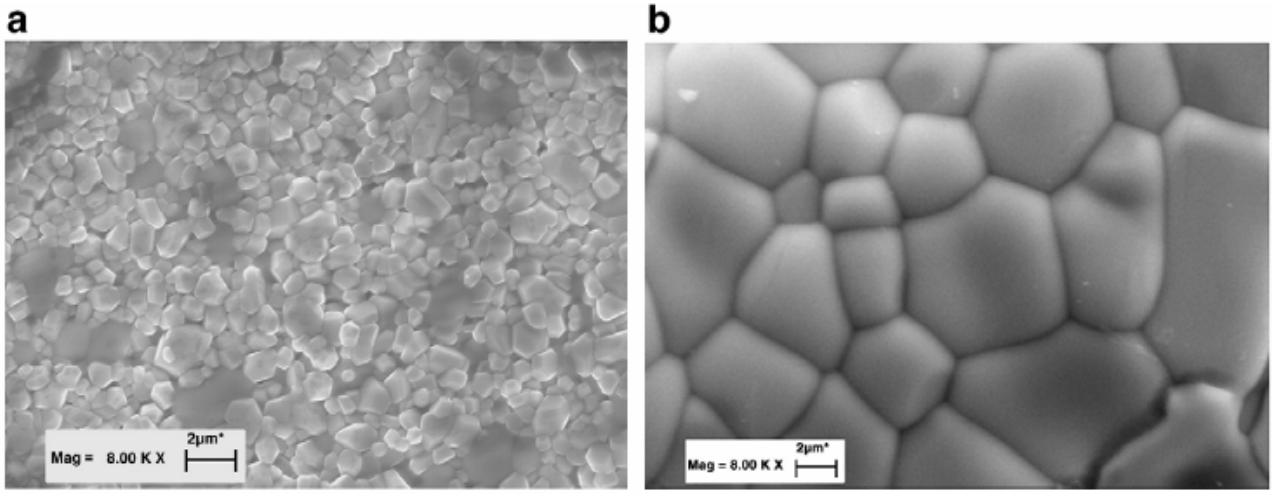

Fig. 2.5. SEM images of pellets $BaCe_{0.8-x}Zr_xY_{0.2}O_{3-\delta}$, **(a)** x = 0.8 **(b)** x = 0.0. A major rate of Zr decreases the grain dimensions, therefore increases the grain boundary region. **[fabbri2008]**.

In a perovskite oxide the grain boundaries are more resistive than the bulk. While cerates have a moderately high grain boundary resistivity, in $BaZrO_3$ this parameter deeply influences the overall conductivity, which decreases by one order of magnitude going from a single crystal to small-grained powder. The BaO demixing in the grain boundary region of $BaZrO_3$ is probably at the origin of hydroxyl defects depletion and of reduced proton mobility **[norby2004], [kreuer2003]**.

Even though $BaZrO_3$ and $BaCeO_3$ have not the same crystallographic symmetry, they have a complete solubility. Recently Fabbri et al. have studied $BaCe_{0.8-x}Zr_xY_{0.2}O_{3-\delta}$ perovskites in order to find a compromise between the chemical stability of zirconates and the moderate grain boundary resistivity of cerates. A higher Zr concentration decreases the grain size and therefore increases the grain boundary region **(Fig. 2.5)**. The conductivity in wet H_2 atmosphere decreases as a function of Zr amount **(Fig. 2.6)**, therefore in these perovskites an increase of grain boundary region involves a decrease of proton conductivity **[fabbri2008]**.

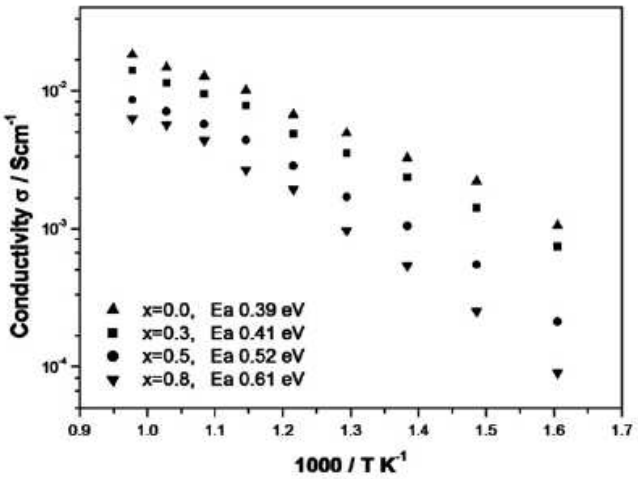

Fig. 2.6. Arrehenius plots of total conductivity in wet H_2 atmosphere for different composition of perovskite $BaCe_{0.8-x}Zr_xY_{0.2}O_{3-\delta}$. **[fabbri2008]**.

3. New ceramic oxide proton conductors

Despite decades of efforts, the research on perovskite oxides proton conductors did not produced significant breakthroughs with respect to the initial discovery of Iwahara and collaborators **[iwahara1981]**; therefore, in the last years new materials are being investigated with the aim of reaching the technological maturity of fuel cell devices based on proton conducting electrolytes. In particular, some oxides whose structure is **characterized by loose tetrahedral moieties have recently attracted considerable interest**. My PhD work and this thesis are inserted in this research activity.

3.1 The proton conductor Ca:$LaNbO_4$

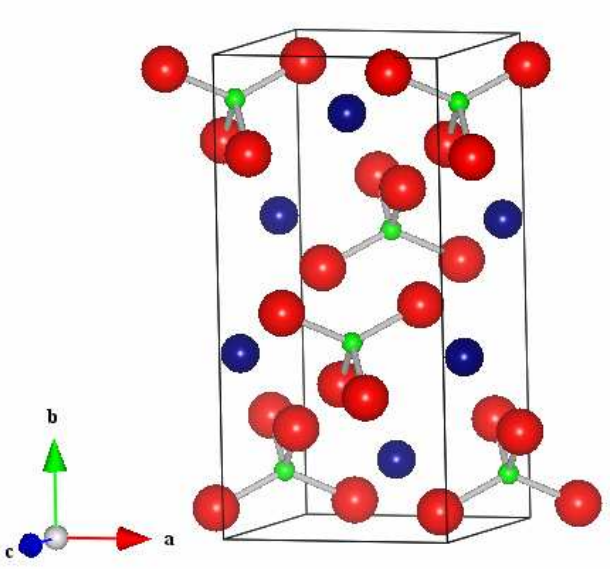

Fig. 3.1. The monoclinic structure of $LaNbO_4$. The smaller Nb^{5+} cations (green balls) reside in isolated tetrahedra of oxygen anions (red balls). The tetrahedra are separated by the bigger La^{3+} cations (blue balls).

Recently Haugsrud, Norby et al. have investigated new proton conductors with chemical formula $RE_{1-x}A_xMO_{4-\delta}$ (RE = Rare Earth, A = Alkaline Earth, M = Nb, Ta). The structure, Fergusonite - type (space group I12/a1) at low temperature (below about 495°C) and Scheelite – type (space group I41/a) at high temperature, is characterized by the presence of **isolated $[NbO_4]$ or $[TaO_4]$ tetrahedra (Fig. 3.1)**. These compounds show a very good chemical stability in CO_2-rich atmospheres **[haugsrud2006a], [haugsrud2007], [mokkelbost2008]** and therefore, despite their low proton conductivity, are considered as a possible alternative to perovskites.

The structure and the phase transitions of $La_{0.99}Ca_{0.01}NbO_{3.995}$ were studied by ***in situ* neutron diffraction (Fig. 3.2)** by Malavasi et al.. The data at 150°C and 300°C are relative to the monoclinic fergusonite structure, while the phase transition to scheelite takes place at about 495°C, probably proceeding throughout a broad range of temperature, where the two phases coexist. In fact, the diffraction pattern at 450°C has been described as a mixture of 75% monoclinic and 25% tetragonal phase. The data at 600°C and 750°C are mainly ascribed to the tetragonal phase, but a minor monoclinic amount can still be detected. This behavior is present in both dry and wet conditions. An important aspect is that the cell volume does not have any abrupt change during the phase transition **[malavasi2009]**, so ensuring mechanical stability of the electrolyte pellets.

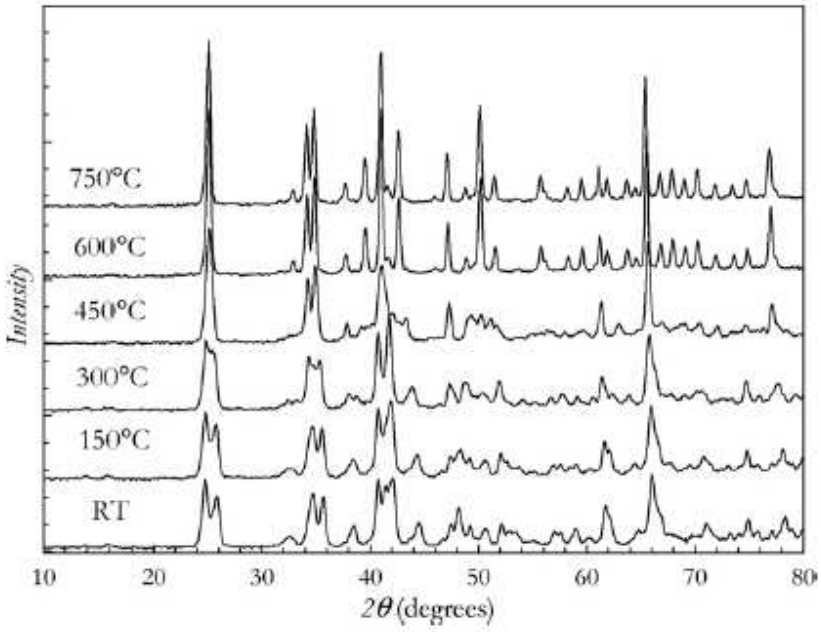

Fig. 3.2. Neutron diffraction patterns of $La_{0.99}Ca_{0.01}NbO_{3.995}$ at different temperatures. At 450°C it is possible to observe the onset of the fergusonite - scheelite phase transition **[malavasi2009]**.

The conductivity of the $RE_{1-x}A_xNbO_{4-\delta}$ (RE = Rare Earth, A = Alkaline Earth) oxides was studied by Haugsrud and Norby. The data of conductivity were collected as a function of oxygen and water partial pressure in a range of temperatures from 300 to 1200°C **(Fig. 3.3)**. Impedance spectroscopy data were also collected in a range of frequencies from 0.5 to 10^6 Hz. At low and moderate temperatures the conductivity of these materials is independent of the oxygen partial pressure, but at high temperatures and oxidizing conditions the total conductivity increases as a function of P_{O2}, showing a contribution of p-type electronic conductivity. The conductivity increases also as a function of P_{H2O} and present the isotope effect in deuterated conditions. It is possible to conclude that the proton conductivity is

dominant in wet atmosphere below 800°C; the highest value is about 10^{-3} S cm^{-1} on the sample $La_{0.99}Ca_{0.01}NbO_{4-\delta}$ and the proton conductivity decreases with decreasing radius of the rare-earth cation. The proton conductivity changes through the phase transition, and in particular the activation energy for the proton mobility increases from 55 kJ mol^{-1} for the high temperature tetragonal phase, to 75 kJ mol^{-1} for the monoclinic one. Impedance spectroscopy data show that only at very low temperatures the grain boundary resistivity is higher than in the bulk, so allowing to conclude that in this material the grain boundary resistivity does not limit the overall performance **[haugsrud2006a], [haugsrud2006b]**.

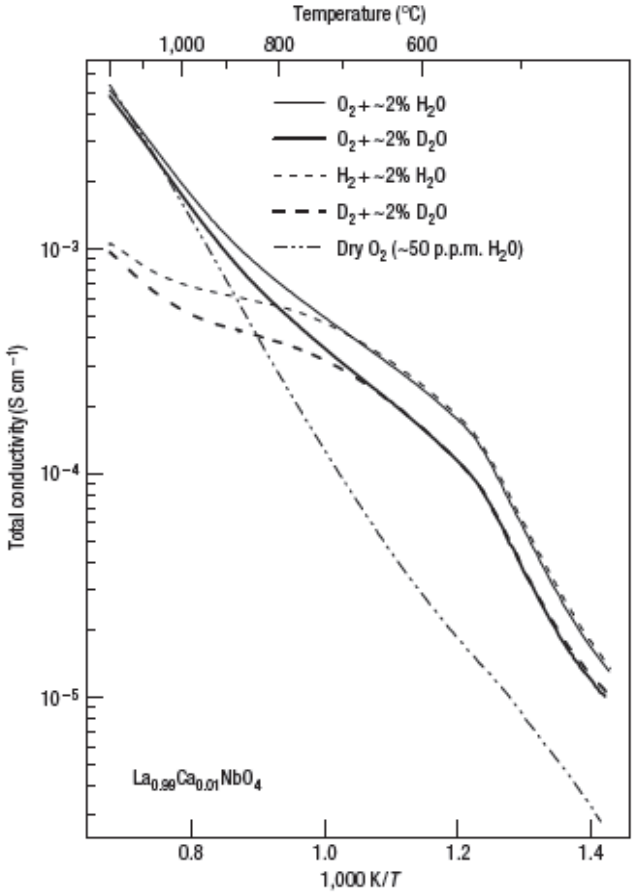

Fig. 3.3. Total conductivity of $La_{0.99}Ca_{0.01}NbO_{3.995}$ in various atmospheres vs. inverse temperature **[haugsrud2006a]**.

Mokkelbost et al. showed that $La_{0.98}Ca_{0.02}NbO_{4-\delta}$ does not have any secondary phase in XRD pattern, and that its morphology is homogeneous with a grain size of 1.2 μm (when sinterized at 1200°C). Increasing of dopant amount in the preparation route does not yield significant change of proton conductivity, but for enhanced grain boundary resistivity; therefore, it is concluded that the solubility of Ca in the bulk of $LaNbO_4$ is probably less than 2% **[mokkelbost2007], [mokkelbost2008]**.

3.2 The proton conductor $LaBaGaO_4$

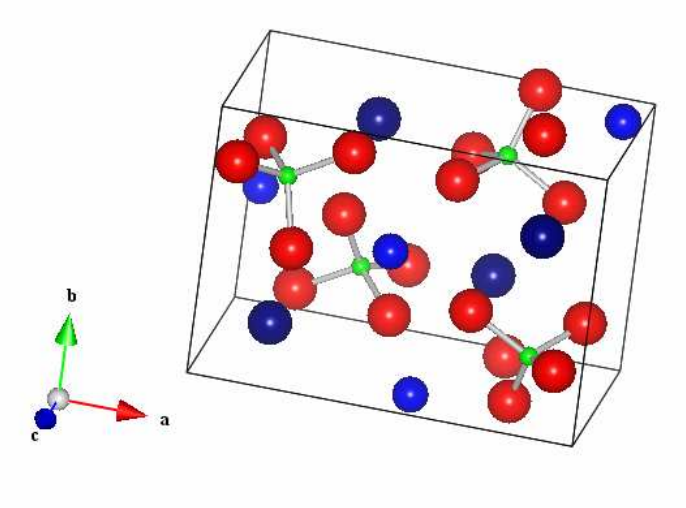

Fig. 3.4. The orthorhombic structure of $LaBaGaO_4$. The Ga^{3+} cations (green balls) reside in isolated and distorted tetrahedra of oxygen anions (red balls). The tetrahedra are separated by La^{3+} cations (deep blue balls) and Ba^{2+} (light blue balls).

A further proton conducting ceramic oxide characterized by loose tetrahedral moieties is $RE_{1-x}Ba_{1+x}GaO_{4-\delta}$ (RE = Rare Earth), whose structure and conductivity were investigated by Kendrick, Slater et al.. The structure is orthorhombic, consisting of **distorted and isolated $[GaO_4]$ tetrahedra** separated by large La^{3+} and Ba^{2+} cations **(Fig. 3.4)**. The ratio La/Ba can be varied to form oxygen vacancies, giving rise to single phase $La_{1-x}Ba_{1+x}GaO_{4-\delta}$ ($0 \leq x \leq 0.2$), as demonstrated by XRD and neutron diffraction data. An expansion of cell parameters (space group $P2_12_12_1$) was observed on increasing the Ba content, because the Ba^{2+} cation is larger than La^{3+} **[kendrick2007],[schönberger2005]**.

Conductivity data were collected as a function of temperature and at different partial pressures of oxygen and water **(Fig. 3.5)**. The conductivity of $La_{0.8}Ba_{1.2}GaO_{3.90}$ is higher in wet atmospheres, with larger difference with respect to dry environment below 650°C. Conductivities measured in deuterated conditions show isotope effect, consistent with proton conduction. The proton conductivity of $La_{0.8}Ba_{1.2}GaO_{3.9}$ is about 10^{-4} S cm^{-1} at 500°C in wet conditions. The conductivity in dry N_2 atmosphere is lower than in dry O_2 atmosphere, so that some electronic p-type conduction is present **[schönberger2005], [li2003]**.

The conductivity of the sample $Pr_{0.9}Ba_{1.1}GaO_{3.95}$ is higher then $La_{0.8}Ba_{1.2}GaO_{3.9}$ ($7.6*10^{-4}$ S cm^{-1} at 500°C in O_2). However, $Pr_{0.9}Ba_{1.1}GaO_{3.95}$ shows substantially electronic p-type conductivity **[schönberger2005]**.

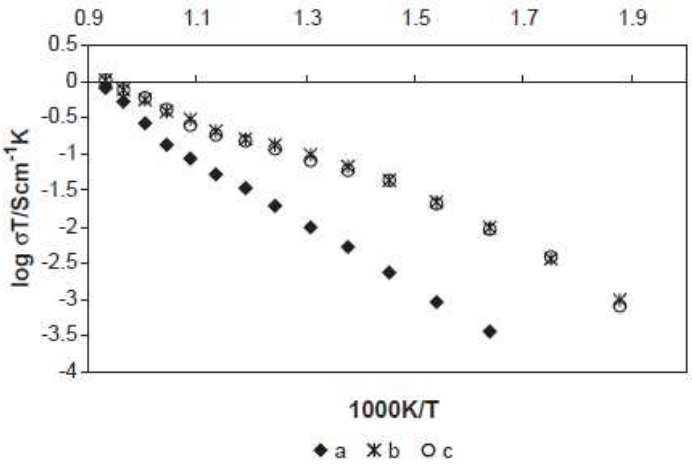

Fig. 3.5. Conductivity data vs. 1/T for $La_{0.8}Ba_{1.2}GaO_{3.90}$ in **(a)** dry N_2, **(b)** wet N_2, **(c)** wet H_2/Ar (5%:95%) **[schönberger2005]**.

The structure of wet (with hydroxyl defects) and dry (with anionic vacancies) $La_{0.8}Ba_{1.2}GaO_{3.90}$ has been investigated by neutron diffraction and DFT computational simulations. For the dry sample the formation of Ga_2O_7 clusters was proposed, originated by the rearrangement of the structure around the anionic vacancies **(Fig. 3.6)**. The migration of oxide ions could take place by breaking and re-forming of Ga_2O_7 clusters along the crystallographic *c* direction, with activation energy of 0.59 eV. The computational analysis showed a significant rotational motion of tetrahedra in the *ab* crystallographic plane.

In the wet samples, the preferred site for the proton was calculated in the interstitial region between O_1 and O_4. The calculated activation energy of inter-tetrahedral proton migration was much lower (0.07 eV) than intra-tetrahedral proton hopping barrier (0.75 eV). **[kendrick2007]**.

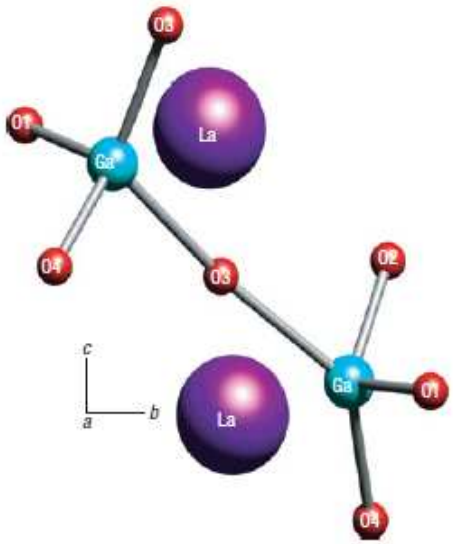

Fig. 3.6. The Ga_2O_7 cluster proposed by Kendrick, Slater et al. in dry-$La_{0.8}Ba_{1.2}GaO_{3.90}$, originated by the rearrangement of two tetrahedral units around the anionic vacancy **[kendrick2007]**.

4. Experimental techniques

In this chapter I'm giving a brief account about the characterization techniques exploited in my PhD work. Some of these techniques (XRD, EXAFS) are devoted to the structural characterization, while TGA and IS are necessary for the functional characterization of the investigated materials. Some details about data analysis are also given.

4.1 Thermogravimetric analysis

The thermogravimetric analysis **(TGA)** allows to study the chemical and physical processes involving sample change of weight in heating/cooling cycles. So, it is possible to investigate the decomposition of solids, and the interactions with gases that involve a change of mass, such as corrosion or gas absorption. In particular, the dissociative incorporation of water in a solid proton conductor involves a weight increase, which can be studied by TGA **[kreuer1999]**.

A TGA apparatus consists of an electronic microbalance that measures the change of weight of a sample put into a furnace and subjected to programmed temperature ramps in a controlled environment. The heating source is usually provided by infrared lamps focused onto the sample, allowing a virtually instantaneous heat transfer, and reaching temperatures as high as 1000°C. A flowing N_2 atmosphere allows to remove the reaction products and acts as coolant for the balance. A sensor is used to detect deviations of the microbalance from the null-point; before each measurement it is important to set up the null-point with a tare measure. **[brown2001]**.

An important factor that affects the microbalance is the variable **buoyancy** of the sample - sample holder system, due to change in density of the fluxed gas as a function of temperature. The hydrostatic force of Archimede in a gas is given by equation:

(4.01) $$F_A = \frac{Pm}{RT} gV$$

where P is the pressure, V is the volume of the sample-sample holder system, m is the molar mass of gas, g is the gravity acceleration, R is the universal constant of gases and T the temperature. The increment of temperature involves a decrease of Archimede's force and, consequently, a little weight increase; then, for samples subjected to very small weight changes, allowance for buoyancy is needed **[brown2001]**.

4.2 X-ray Diffraction and Rietveld analysis

In 1913 L. Bragg wrote the Bragg's law for x-rays constructive interference in a crystal, and in the same years L. Bragg and M. von Laue were the first to use the x-ray diffraction **(XRD)** to investigate the structure of crystals, in particular they found the structure of some simple crystal **[viterbo2003]**.

Nowadays the x-rays diffraction gives important contributions about study of solid structure in material science. As is written in second chapter of this thesis some important properties of proton conductors are strongly influenced by the structure, so XRD is a very useful technique to study this compound **[giannici2007a]**.

The XRD technique is based on the interference between the X-rays beams scattered by the atoms of crystal.

The electron density of a real crystal can be thought as the convolution of cell electron density ($\rho_0(\boldsymbol{r})$) with its periodicity function, all multiplied by the form factor of cell ($\phi(\boldsymbol{r})$):

(4.02) $$\rho_e(\bar{r}) = \left[\rho_0(\bar{r}) * \sum_{u,v.w} \delta(\bar{r} - \bar{R}_{u,v,w}) \right] \phi(\bar{r})$$

Where *u, v, w* are the vector that define the real Bravais's lattice ($\boldsymbol{R}_{u,v,w}$). The value of cell form factor ($\phi(\boldsymbol{r})$) is one inside de volume of cell and zero outside.

The scattered amplitude is given by the Fuorier transform of electron density:

(4.03) $$F(\bar{q}) = FT[\rho_e(\bar{r})] = \frac{1}{V} F(\bar{H}) \sum_{h,k,l} \phi(\bar{q} - \bar{H}_{h,k,l})$$

Where *h, k, l* are the vector that define the reciprocal lattice ($\boldsymbol{H}_{h,k,l}$) and $\boldsymbol{q}$ is the scattering vector.

The intensity of scattered beam, the information received from the experiment, will be:

(4.04) $$I(\bar{q}) = \left| \frac{1}{V} F(\bar{H}) \sum_{h,k,l} \phi(\bar{q} - \bar{H}_{h,k,l}) \right|^2$$

The atomic coordinates would given from the scattered amplitude, unfortunately the diffraction experiments only give the diffracted intensities, which are proportional to the square of the amplitudes, so the information about the phase of complex numbers is lost. In crystallography it is called **the phase problem**.

The thermal vibration of atoms around the position of minimum energy produces an effective increase of the electronic density distribution width. A Gaussian and isotropic distribution of electronic density is often assumed. If *U* is the mean square displacement of

atom around the position of minimum energy then the Fourier transform of electronic density will be:

(4.05) $FT[\rho_e(\bar{r})] = \exp(-8\pi^2 U \sin^2\theta/\lambda^2) = \exp(-B\sin^2\theta/\lambda^2)$

where B is the Debye-Waller disorder factor.

If we take account the temperature the atomic scattering factor becomes:

(4.06) $f_T = f_0 \exp(-B\sin^2\theta/\lambda^2)$

where f_0 is the atomic scattering factor at T = 0.

[viterbo2003].

A crystalline powder is formed by a very large number of randomly oriented small crystals (**crystallites**) (in the **Fig. 4.4** an example of powder diffraction pattern). Each reciprocal lattice vector will assume a large number of randomly possible orientations. As a consequence, the observed XRD pattern is a function of the 2θ angle between the scattered and the incident beam or, more rigorously, of the wavevector modulus difference *q* between the scattered and the incident beam:

(4.07) $|\mathbf{q}| = q = \frac{2\sin\theta}{\lambda}$

The **Rietveld method** allows to carry out a structural refinement using the full diffraction pattern. The XRD pattern is fitted by an array of peak functions (Gaussian, pseudo-Voigt, Pearson or else, depending on the exploited experimental apparatus) whose angular position depends on the unit cell parameters and whose intensity is a function of the unit cell content (atomic positions in the asymmetric unit, space group symmetry, thermal disorder etc.). A least-squares refinement is performed by minimizing the function:

(4.08) $S(q_i) = \sum_j w_j [I_{obs}(q_i) - (I_{calc,j}(q_i) + I_{back}(q_i))]^2$

where $I_{obs}(q)$ is the observed intensity, $I_{calc,j}(q)$ is the contribution of the *j*-th peak function to the overall calculated intensity and $I_{back}(q)$ is the background function, usually simulated by a polynomial of suitable degree.

In conclusion, the application of the Rietveld refinement needs a structural model, given by the reference structure of the investigated material and, within this model, allows to determine, for a given material, specific information such as the cell parameters, the refined atomic position with static or dynamic thermal disorder, the site occupancy relative to the assumed space group and, therefore, also the doping amount of a given crystallographic site.

[viterbo2003]

The most popular package for the Rietveld refinement is **GSAS**, allowing to simultaneously refine several crystal phases, with a quantitative determination of relative phase amount, crystallite size and possible preferred orientations **[toby2001]**.

4.3 Synchrotron radiation

The Maxwell's equations imply that an accelerated charged particle generates electromagnetic radiation. This fact is at the basis of the X-ray production in the synchrotron facilities: bunches of electrons are **accelerated to relativistic velocities**, usually by a linear accelerator (Linac) and a first booster synchrotron, and injected in the ultra-high-vacuum synchrotron ring. The electrons are bound to run in the synchrotron ring by bending magnets, so inducing the emission of synchrotron radiation. As the electrons have a speed close to light, the relativistic time contraction brings the synchrotron radiation into the X-ray band of frequencies. **[margaritondo2003]** Moreover, the bunches of electrons can be forced to cross periodic structures of magnets **(Fig. 4.1)**, the **undulators** and the **wigglers**, that accelerate the electrons, the former with long pulses and the latter with short pulses, giving rise to a very brilliant and collimated x-ray beam.

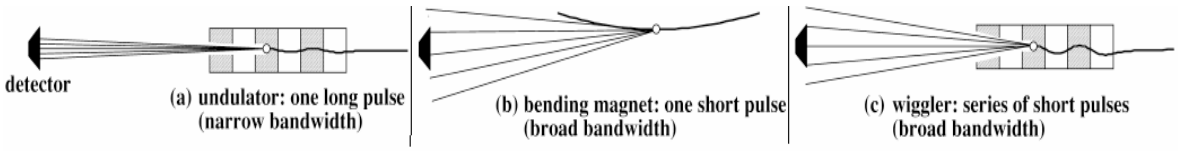

Fig. 4.1. In a synchrotron **undulators (a)** and **wigglers (c)** accelerate the electrons with long pulses and with short pulses producing, respectively, narrow and broad energy spectrum. The **bending magnets (b)** bend the electrons **[margaritondo2001]**.

The characteristics of synchrotron radiation are:

- high intensity
- high brilliance of the source
- high rate signal / noise
- narrow angular collimation
- high degree of polarization
- pulsed time structure
- high beam stability

Fig. 4.2. **ESRF**, Grenoble, one of the biggest and must powerful synchrotrons in the world. **[ESRF]**.

The 3rd generation synchrotrons are characterized by very high (GeV) electron energies and highly advanced control techniques. The biggest and most powerful synchrotrons in the world are: Spring-8 (8 GeV) in Japan, APS (7GeV) in U.S.A. and ESRF (6 GeV) in France **(Fig. 4.2)**; and in a near future Petra-III in Germany.

4.3.1 Synchrotron radiation and X-ray Diffraction

XRD experiments carried out at a synchrotron beamline take advantage of a much better signal-to-noise ratio and instrumental resolution with respect to laboratory instrumentation. Therefore, phase identification is more reliable, and impurity phases can be easily detected. The very small instrumental contribution to the peak broadening and the high brilliance make possible to expand the range of measurable crystallite size and to analyze the structure of nanophases. **Fig. 4.3** shows the differences between a powder diffraction pattern collected in a synchrotron and a diffraction pattern, of the same ceramic powder, collected in laboratory.

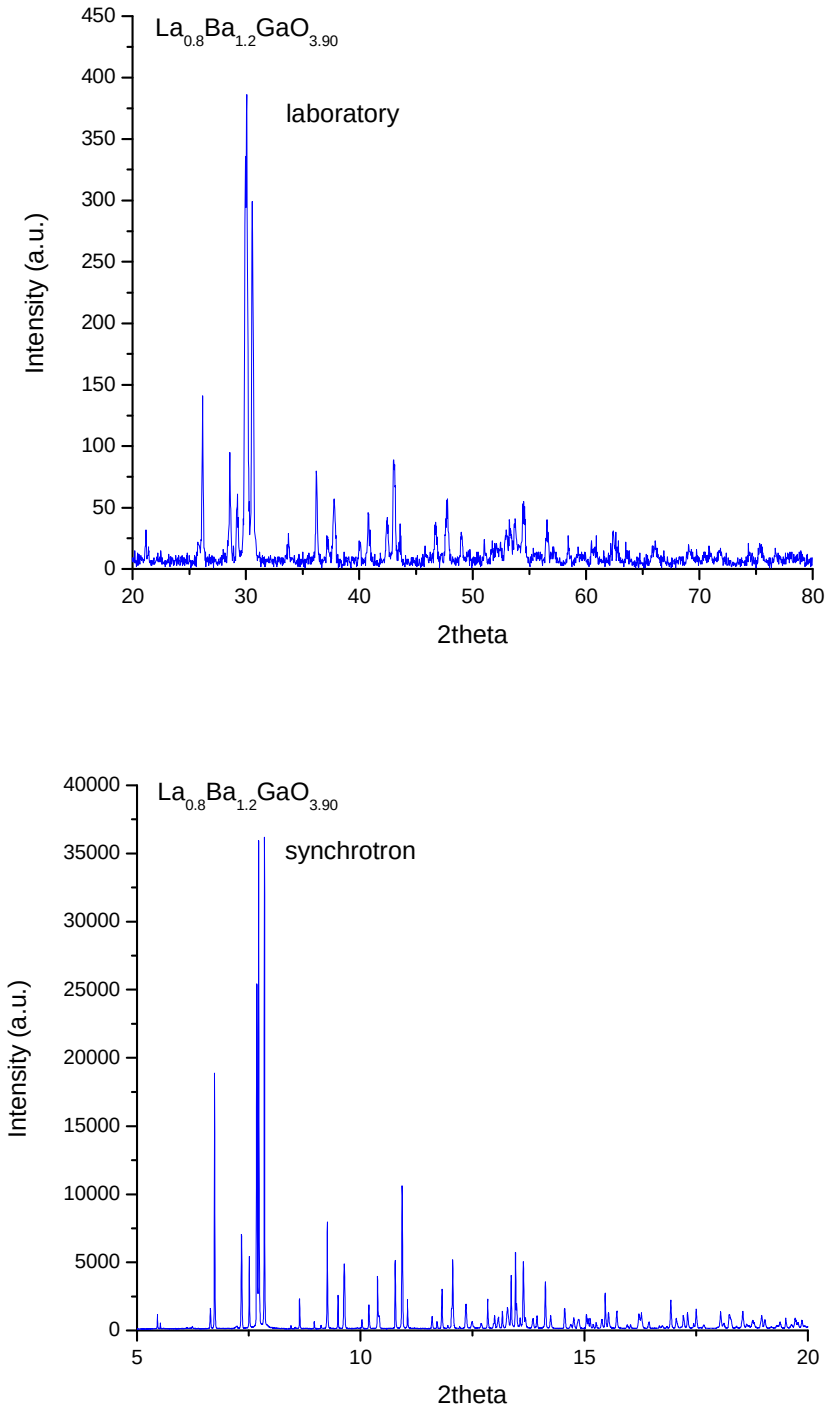

Fig. 4.3. Comparison between the diffraction pattern of sample $La_{0.8}Ba_{1.2}GaO_{3.90}$ collected at the XRD laboratory of ISMN-CNR in Palermo (above) and the diffraction pattern of the same sample collected at beamline ID31 of ESRF (below).

Synchrotron radiation gives the opportunity of performing in the most effective experimental conditions *in situ* XRD experiments, collected as a function of **temperature** (*temperature-resolved experiments*), **pressure** (*pressure-resolved experiments*), **time** (*time-resolved experiments*), or **electric/magnetic field**. It is also possible to investigate the **chemical**

properties of samples, for example in a gas-solid reaction, by creating a suitable chemical environment in the sample holder and collecting XRD patterns that allow to monitor a chemical reaction involving a structural change of the solid. *In situ* experiments require non-standard instrumentation, but also a careful planning of the experiment, taking into account the limiting cases of: a) data collection time slower than the structure transition (in this case the sample an only be studied at equilibrium), b) data collection time faster than the structure transition (therefore allowing to follow in details the development of the event) **[artioli2003]**.

4.3.2 X-ray Absorption Fine Structure (XAFS)

X-ray absorption spectroscopy can be effectively applied to the structural characterization of materials only exploiting a synchrotron radiation source.

When a X-ray beam crosses a sample of thickness x the intensity (I) is reduced according to the law:

(4.09) $I = I_0 \exp(-\mu x)$

where μ is the **linear absorption coefficient** that depends on the density and composition of the sample, but also on the X-ray energy: when the energy increases, μ progressively decreases. In this behavior there are the sharp discontinuities, called **absorption edges**, occurring in correspondence of the photon energies, peculiar of a given atomic species, high enough to eject an electron from a core atomic level **(Tab. 4.1).**

Edge:	K	L_1	L_2	L_3	M_1	…
Core level:	1s	2s	$2p_{1/2}$	$2p_{3/2}$	3s	…

Tab. 4.1. Labels of the absorption edges corresponding to the indicated atomic core levels

The emitted photoelectron wave number is:

(4.10) $k = \sqrt{(2m/\hbar^2)(\hbar\omega - E_b)}$

where E_b is the core electron binding energy.

If the absorber atom is not isolated, the photoelectron wave is backscattered by its neighboring atoms and gives rise to an interference pattern by superposition with the incoming photoelectron wave. **(Fig. 4.4)** As a consequence, the absorption coefficient exhibits a fine structure depending on the energy of the photoelectron, called **EXAFS** (*Extended X-rays absorption fine structure*), that brings information about the nature, the position and the number of backscatterer atoms. Therefore, the EXAFS spectroscopy is

selective for chemical species and constitutes a powerful tool to investigate the structure around an absorber atom. As the photoelectron mean free path is limited to a few ångstroms, the structural analysis is limited to the closer coordination shells about the absorber.

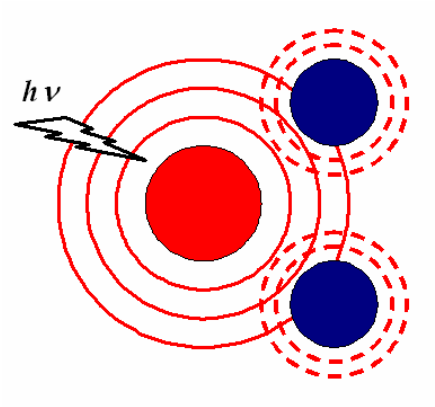

Fig. 4.4. Schematic picture of EXAFS phenomenon. When a X-ray photon of enough high energy is absorbed by an atom, a core level electron is ejected; this photo-electron can be described by a spherical wave. If the emitting atom is not isolated the photoelectron will be back-scattered by neighboring atoms

Fig. 4.5 reports the complete K absorption edge of Ga in the $LaBaGaO_4$ oxide: the overall XAFS (X-ray Absorption Fine Structure) is divided into two regions:

- The oscillations of the absorption coefficients limited in the 30-50 eV interval above the edge are called **XANES** (*x-rays absorption near edge structure*). The XANES allows to obtain informations about the electronic structure and the oxidation state of the absorber.
- The μ oscillations from the XANES to about 1 keV beyond the edge constitute the **EXAFS**. **[fornasini2003].**

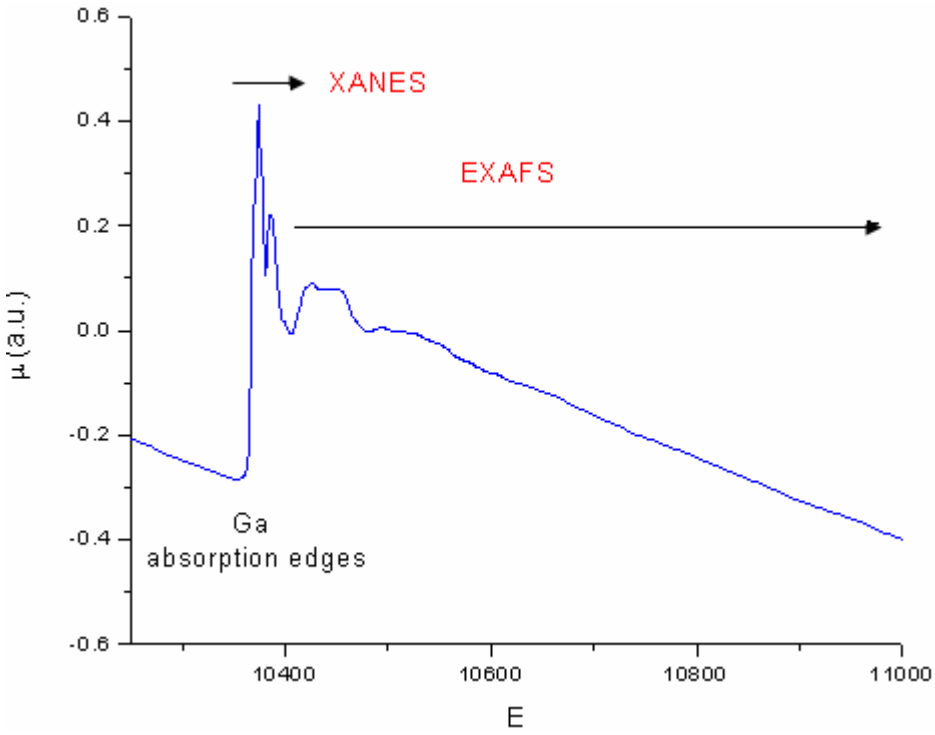

Fig. 4.5. X-rays absorption fine structure **(XAFS)** at the K edge of Ga for the sample $LaBaGaO_4$. The two regions **XANES** and **EXAFS** are shown.

The absorption coefficient $\mu(\omega)$, as a function of the photon energy $E = \hbar\omega$, depends on the probabilities of transition from the initial $|\psi_i^{N-1}\psi_i>$ to the final electronic state $|\psi_f^{N-1}\psi_f>$:

(4.11) $$\mu(\omega) \propto S_0^{\,2} \left| < \psi_i \mid \hat{\eta}\bar{r} \mid \psi_f > \right|^2$$

where

(4.12) $$S_0^{\,2} = \left| < \psi_i^{N-1} \mid \psi_f^{N-1} > \right|^2$$

Therefore, it is assumed that the interaction involves just one electron, with initial state $|\psi_i>$ corresponding to the core atomic state and final state $|\psi_f>$ representing the photoelectron wavefunction. The other N-1 electron are passive with respect to the interaction with the incoming photon, with initial state $|\psi_i^{N-1}>$ corresponding to the electronic state of the unperturbed N-1 atomic electrons and final state corresponding to the relaxed system of the N-1 electrons. S_0^2 is the superposition integral of the N-1 electrons wavefunction and its value is generally between 0.7 and 0.9. **Eq. 4.11** is derived in the electric dipole approximation and therefore $\hat{\eta}$ represents the polarization unit vector.

The EXAFS function is defined as the difference between the actual absorption coefficient μ and the absorption coefficient of the isolated atom μ_0, normalized to μ_0:

(4.13) $$\chi(k) = \frac{\mu - \mu_0}{\mu_0}$$

The standard EXAFS formula is:

(4.14) $$\chi(k,T)=\sum_j \frac{S_0^{\,2} N_j \left| f_j(k) \right|}{k\bar{r}_j^{\,2}} \exp(-2\bar{r}_j/\lambda_j)\exp(-2k^2\sigma_j^{\,2})\sin(2k\bar{r}_j+\phi_j(k))$$

where $f_j(k)$ is the backscattering amplitude of the j^{th} backscatterer, r_j the distance from the absorber, N_j the number of backscatterers located at a distance r_j from the absorber. The first exponential factor describes the anelastic losses, with λ_j representing the mean free path of the photoelectron. The second exponential factor takes into account the fluctuation of the local structure, both originated by the thermal motion of atoms and by the structural disorder due to the distribution of interatomic distances. The disorder is treated within the harmonic approximation, assuming a Gaussian distribution about the average; the σ_j^2 parameter is called Debye-Waller factor. The interference term $sin(2k\mathbf{r_j}+\phi_j(k))$ in the EXAFS formula takes into account the relative position of absorber and backscatterer and the $\phi_j(k)$ phase-shift between the emitted and the backscattered wave. **[fornasini2003]**

Giving important information about the local structure of the sample, EXAFS is a useful technique to investigate the local structural changes due to the water incorporation in a solid oxide proton conductor **[giannici2007a]**.

The first step in the EXAFS data analysis is **the extraction of the EXAFS signal** from the collected data **(Fig. 4.6)**:

(4.15) $$\mu x = \ln(I_0/I) - \mu_n x$$

Where x is the sample thickness, $\mu_n x$ is the background, resulting from the contribution of all the excitations of the selected elements and of other elements; it can be estimated by extrapolating the pre-edge behavior. A threshold energy E_s is usually chosen in correspondence of the first inflection point of the edge and the discrepancy between E_s and the electron binding energy E_b in **eq. 4.10** is called E_0 and treated as a free parameter to optimize the best-fit.

The next step is the calculation of the **Fourier Transform** to go from the wavenumber k space to the r space of distances from the absorber **(Fig.3.7)**:

(4.16) $$F(r)=\int_{k\,\min}^{k\,\max} \chi(k)W(k)k^n \exp(2ikr)dk$$

where W(k) is a window function which reduces the spurious oscillations induced by the finite k range and the term k^n is used to balance the low and high k-parts of the spectrum.

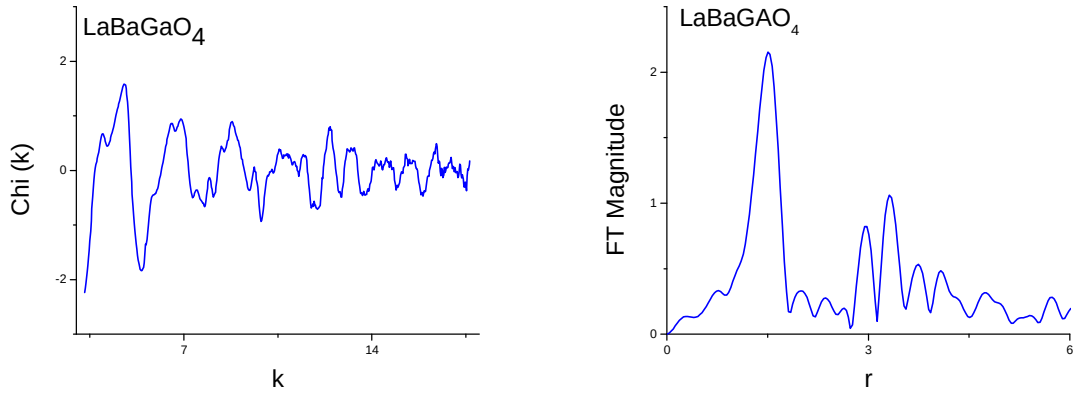

Fig. 4.6. Extracted EXAFS signal of a $LaBaGaO_4$ sample (left); modulus of the corresponding Fourier Transform (right).

To model the EXAFS signal, a geometrical structure around the absorber atom is assumed and **all significant photoelectron scattering paths and in particular also multiple scattering paths (Fig. 4.7)** are taken into account. To this concern, one of the most popular software packages is **FEFF [klementev2001]**.

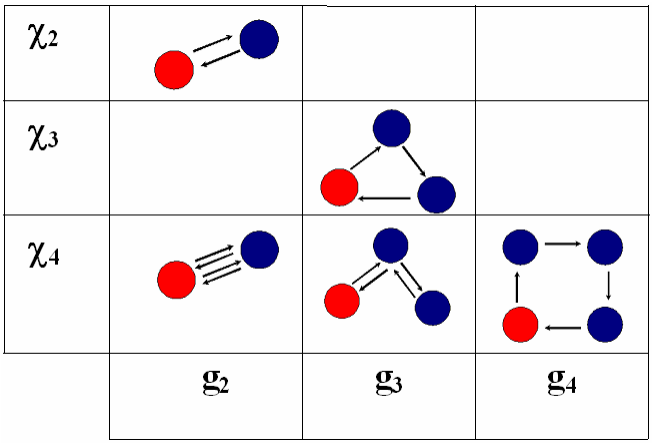

Fig. 4.7. Examples of multiple scattering paths. Each row corresponds to a given contribution χ_n. Each column corresponds to a given n-body correlation function g_n. **[fornasini2003]**

Finally, a **fitting refinement** is carried out. The maximum number of independent parameters that can be refined over a given data set is:

(4.17) $$n_{ind} = \frac{2\Delta k \Delta r}{\pi}$$

[fornasini2003]

4.4 Electrochemical Impedance Spectroscopy

The concept of electrical impedance was first introduced by Oliver Heaviside in the 1880s. Nowadays **EIS** (Electrochemical Impedance Spectroscopy) is a powerful technique to characterize the electrochemical behavior of materials and its microscopic regions. In particular, EIS is very important to characterize the solid oxide proton conductors **[potter2006]**.

In this technique, AC impedance measurements are made in a wide range of frequencies (usually **from 10^{-2} to 10^{7} Hz**) and **the different regions of a material are characterized according to their relaxation times**. The measurements are usually taken from a cell having two identical thin electrodes applied to the faces of a simple electrolyte pellet. The flow of electrons, protons or other charged particles depends on the impedance of the electrodes and of the electrolyte. The flow may depend on structural inhomogeneities of the electrolyte, such as grain boundary, minority phases or defects in the bulk. The impedance of a material is determined in **different atmospheres** (inert, oxidant or reducing, dry or wet atmospheres) and as a function of **temperature** and/or **applied pressure** **[macdonald,johnson2005], [irvine1990]**.

When an AC ν(t) signal:

(4.18) $v(t) = V_m \sin(t\omega)$

is applied to a cell, the measured current *i(t):*

(4.19) $i(t) = I_m \sin(t\omega + \theta)$

has a phase delay θ, which is zero for purely resistive behavior.

The response of the cell is given by **eq. 4.20** if it is purely resistive, by **eq. 4.21** if it is capacitive, by **eq. 4.22** if it is inductive:

(4.20) $i(t) = \frac{v(t)}{R}$

(4.21) $i(t) = [dv(t)/dt]C$

(4.22) $i(t) = [dv(t)/dt]\frac{1}{L}$

Where *R*, *C* and *L* are respectively the resistance, the capacity and the inductance.

The Fourier transform can simplify significantly the mathematical treatment of system giving a relation similar to Ohm's law:

(4.23) $I(j\omega) = \frac{V(j\omega)}{Z(j\omega)}$

where j is the imaginary unit and ***Z(jω)* is the "impedance function"**. For each type of circuit element the impedance has a different value **(Tab. 4.2)**.

Circuit element	Impedance Z(jω)
Resistance	R
Capacity	$1/j \cdot \omega \cdot C$
Inductance	$j \cdot \omega \cdot L$

Tab. 4.2. Are given the value of Impedance for each type of circuit element.

The impedance is a complex quantity with a real part (resistive) *Z'* and an imaginary part (capacitive/inductive) *Z''*:

(4.24) $Z(j\omega) = Z' + jZ''$

(4.25) $\mathrm{Re}(Z) = Z' = |Z|\cos(\theta)$ and $\mathrm{Im}(Z) = Z'' = |Z|\sin(\theta)$

with the phase angle:

(4.26) $\theta = \tan^{-1}\left(\frac{Z''}{Z'}\right)$

[macdonald,johnson2005].

The analysis of impedance data is made by fitting with a mathematical model; it is based on an **equivalent circuit made up of ideal resistors, capacitors and inductances**. Different regions of a ceramic oxide are usually fitted by resistances and capacitances placed in parallel **(Fig. 4.8)**.

As a useful example, the impedance of a (R_1 + Parallel R_2-C) circuit is:

(4.27) $Z(j\omega) = R_1 + \frac{1}{(1/R_2) + (j\omega C)}$

A software package used for EIS data analysis is **ZSimpWin**.

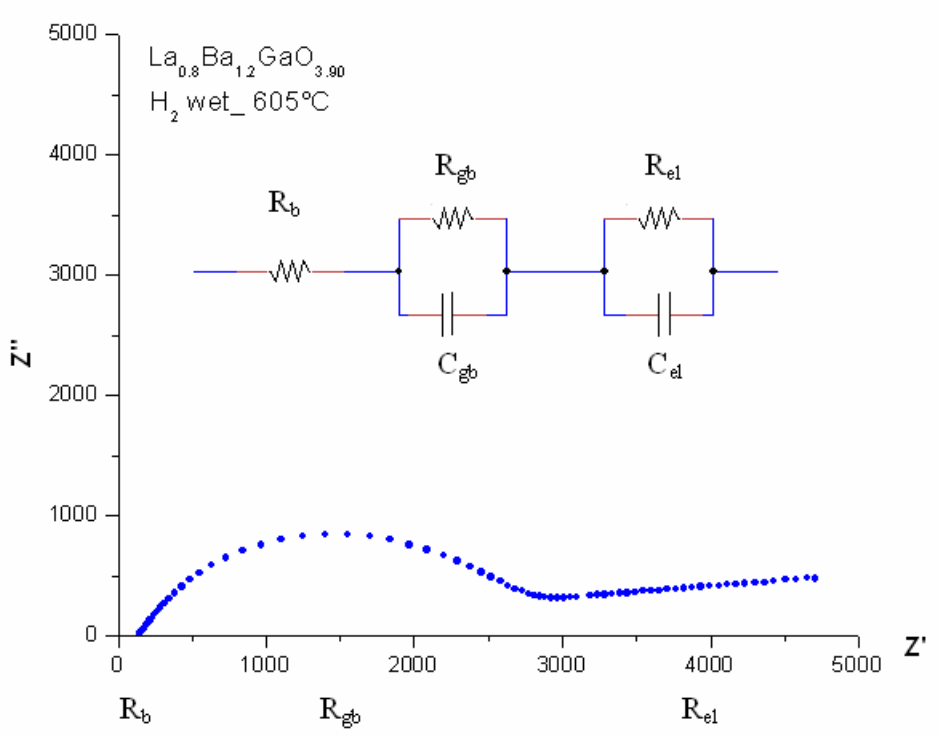

Fig. 4.8. Impedance spectroscopy data of sample $La_{0.8}Ba_{1.2}GaO_{3.90}$ (collected at 605°C in H_2 wet atmosphere) and relative equivalent circuit.

The real component of impedance is resistive: from the value of frequency at the maximum we can calculate the value of capacitor:

(4.28) $2\pi\upsilon_{max}RC = 1$

The next stage is to assign *R* and *C* values to regions of cell, Irvine et al. have gave a useful table of possible interpretations for different capacitance value, see **Tab. 4.3**. **[irvine1990]**

Capacitance [F]	**Phenomenon Responsible**
10^{-12}	Bulk
10^{-11}	Minor second phase
10^{-11}-10^{-8}	Grain boundary
10^{-10}-10^{-9}	Bulk ferroelectric
10^{-9}-10^{-7}	Surface layer

Tab. 4.3. Capacitance values and their possible interpretations **[irvine1990]**.

The disadvantage of EIS is associated with the possible ambiguities in interpretation, as different ideal circuit model can give the same impedance spectrum. To overcome these ambiguities, it is important, to analyze carefully **several sets of measurements** in different conditions **[macdonald,johnson2005]**.

5. Experiments & Results

5.1 Introduction

As discussed in the third chapter, great interest has been recently devoted to a new generation of proton conductor oxides, characterized by a structure having loose tetrahedral moieties.

$La_{1-x}Ba_{1+x}GaO_{4-x/2}$ have been proposed as proton conductor by Slater et al. **[kendrick2007], [schönberger2005], [li2003].** During my PhD work, I studied the correlation between structure and conductivity of $\mathbf{La_{1-x}Ba_{1+x}GaO_{4-x/2}}$ oxides (x = 0,…0.2). From now on, I will designate this class of compounds with the acronym LBGx, where *x* represents the barium excess. Moreover, aiming at gathering data on proton conduction in materials constituted by loose tetrahedral moieties, also the oxides $\mathbf{Nd_{1-x}Ba_{1+x}GaO_{4-x/2}}$ (from now NBGx) were investigated. The structures of both dry and wet samples, as well as their dependence on temperature, have been investigated by combined high resolution (HR) XRD, *in situ* XRD and EXAFS spectroscopy. Water incorporation was studied by TGA analysis. The proton conductivity and its variation in the microscopic regions of materials was investigated by IS analysis.

5.2 Synthesis

The $RE_{1-x}Ba_{1+x}GaO_{4-x/2}$ (RE = La, Nd) materials were synthesized according to the solid-state reaction method **[kendrick2007]**. Stoichiometric amounts of reactants (La_2O_3 or Nd_2O_3, $BaCO_3$ and Ga_2O_3) were weighed (within an accuracy of 10^{-3}g) and intimately mixed in a mortar. The powder was heated at 1200 °C for 12h and ground in a ball mill for 15 minutes. The powder was again heated at the same temperature and ground, and finally heated another time at 1300°C for 12h and ground. Furthermore, aliquots of the powders were heated at 800°C for 3h under a flow of dry oxygen in order to obtain the dry samples (from now on, referred to by a "*d*" at the end of the acronym, for example LBG5d).

The XRD data, collected with a Bruker D500 laboratory diffractometer (**Fig. 5.1**) and subjected to Rietveld refinement, show that the powders are constituted by the single orthorhombic phase $P2_12_12_1$ **[rueter1990]** in the range of composition:

LBGx, $0 \leq x \leq 0.2$ and NBGx, $0 \leq x \leq 0.05$

Suitable pellets for conductivity measurements were obtained by uniaxial pressing at 250 MPa and subsequent heating at 1350°C for 5h. Pt Electrodes were deposited using a porous platinum paste (Heraeus, CL11-5100), and a gold wire was stuck to both sides of the pellet. The cells were then heated at 800°C for half an hour.

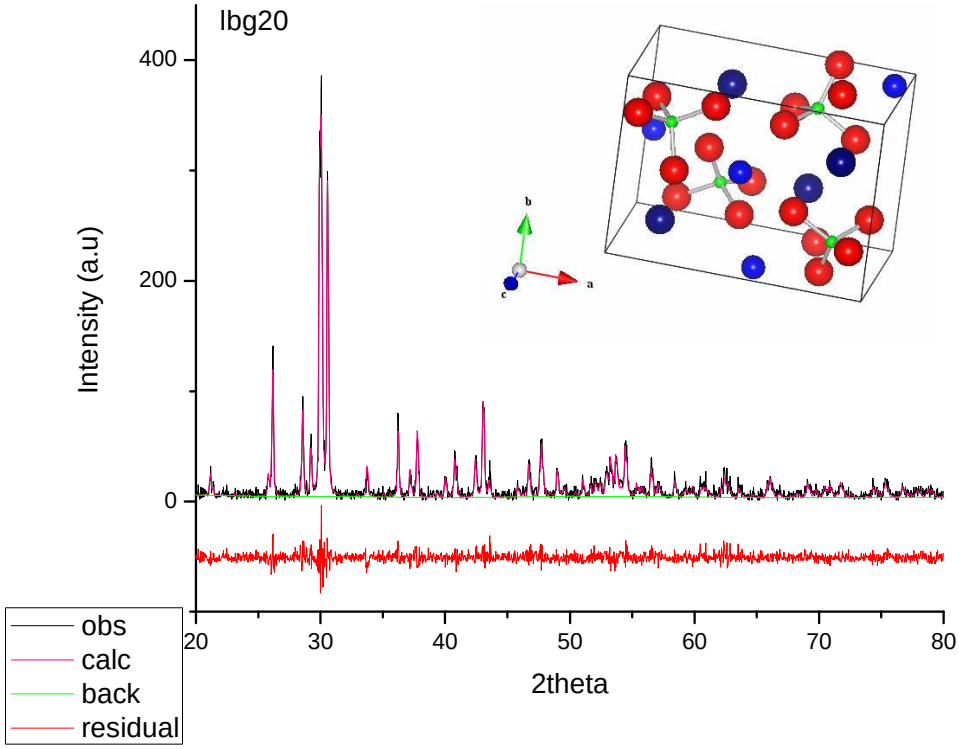

Fig. 5.1. XRD data (black line) and Rietveld refinement (pink line) of LBG20 sample. The powders are constituted by a single orthorhombic phase, S.G. $P2_12_12_1$: the Ga^{3+} cations (green balls) reside in isolated and distorted tetrahedra of oxygen anions (red balls). The tetrahedra are separated by La^{3+} cations (deep blue balls) and Ba^{2+} (light blue balls).

5.3 TGA Analysis

The incorporation of water in the structure of the oxides was studied by means of thermo-gravimetric analysis; data were collected with a TA instruments Q5000IR balance. Measurements were performed under N_2 atmosphere with a slow heating ramp, namely 2.5°C/min (**Fig. 5.2**). A first loss in weight is attributable to the release of CO, CO_2 and H_2O possibly adsorbed on the surface of the powders, as well as observed for other proton conductor oxides, whereas the second loss is due to the water incorporated in the structure **[mokkelbost2007]**. All the LBGx samples start to lose water at about 300°C, whereas the NBG5 sample holds water up to higher temperatures (ca. 550°C). The mole fraction of water

loss is in agreement with the theoretical value expected for the relevant Ba/RE ratio in the structure (**Tab. 5.1**).

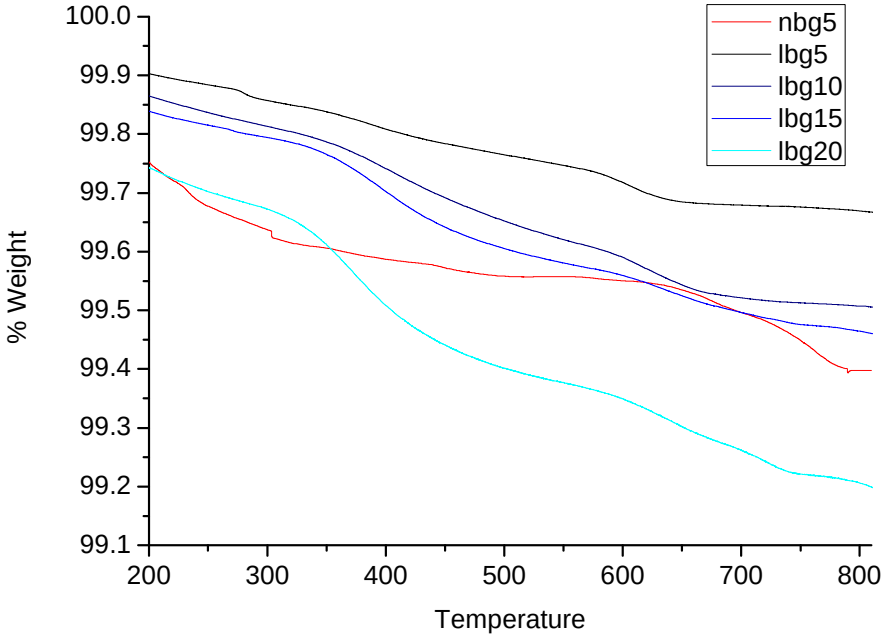

Fig. 5.2. TGA data: All LBGx samples start to lose water at about 300°C, while NBG5 sample holds water at higher temperatures, until about 550°C.

Sample	Water loss (mole fraction) Experimental	Water loss (mole fraction) Theoretical
LBG5	0.037	0.025
LBG10	0.061	0.050
LBG15	0.071	0.075
LBG20	0.103	0.100
NBG5	0.037	0.025

Tab. 5.1. Mole fraction of water loss, measured by TGA, and the theoretical value given from the ratio Ba/RE in the structure. The two values are in fairly good agreement.

Thermochemical parameters for the water loss were determined, from linear regression of lnK vs. 1/T data **(eq. 5.01)**, as large as ΔH^0 = -90 kJ/mol, ΔS^0 = -118 J/mol.

(5.01) $\ln K = T\Delta S^0 - \Delta H^0$

The high and negative value of hydration entropy suggests a significant ordering of the O-H bonds in the lattice.

5.4 *In situ* XRD Analysis

In situ XRD data were collected at the **ID11** beamline of the **ESRF** synchrotron (Grenoble) using a monochromatic radiation with λ = 0.34Å. The sample was mounted in a Linkam thermochemical cell, heated in the range 25°C - 800°C and connected to a gas stream, namely water vapor and N_2 for wetting atmosphere or N_2 for drying atmosphere. Using the GSAS software, all diffraction patterns were satisfactorily modeled in the orthorhombic $P2_12_12_1$ space group **[rüter1990]**. Two typical examples are reported **(Fig. 5.3 – 5.4).**

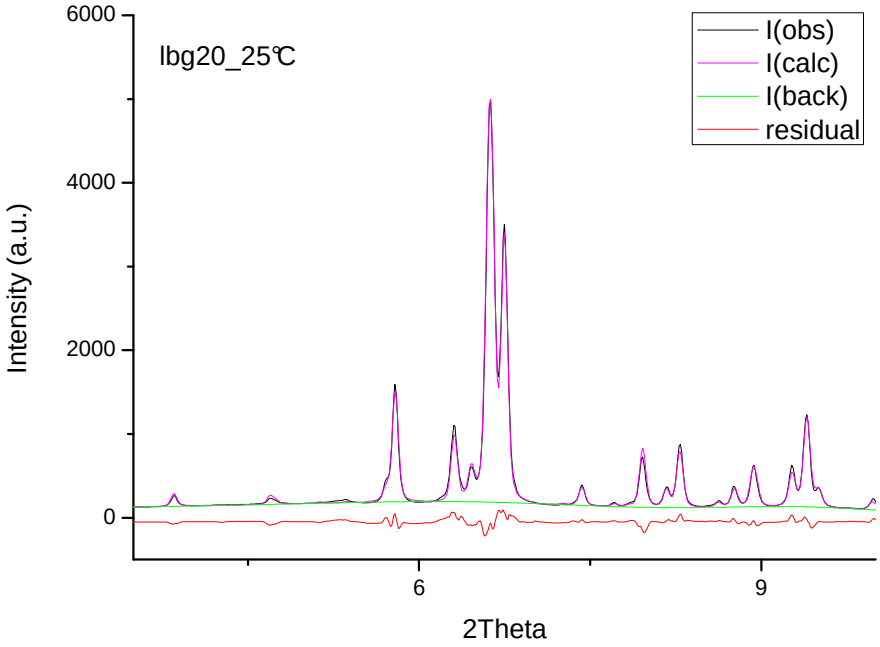

Fig. 5.3. XRD data (black line), measured at 25°C, and Rietveld refinement (pink line) of LBG20 sample. The residual (red line) is the difference between the experimental and calculated pattern.

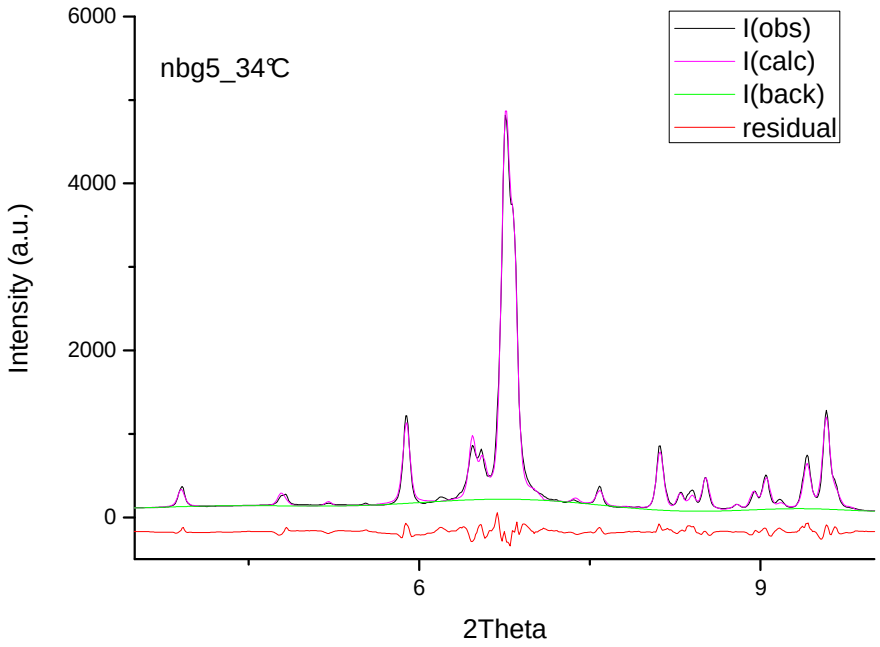

Fig. 5.4. XRD data (black line), measured at 34°C, and Rietveld refinement (pink line) of NBG5 sample. The residual (red line) is the difference between the experimental and calculated pattern.

Analysis of data collected at ca. 30°C shows that the substitution of the La^{3+} or Nd^{3+} cations with the larger Ba^{2+} causes an increase of the cell parameters as a function of the dopant amount. Indeed, we can notice a shift of the diffraction peaks to smaller angles **(Fig. 5.5)**. In particular, if we compare the dry samples, in order to exclude the effects of protonation, a larger elongation is observed along the *a* axis, rather than along the other cell axes **(Tab. 5.2)**. When hydroxyl defects are introduced, i.e. for the wet samples, we can notice a decrease of the *a* parameter, an increase of *b* and a smaller increase of *c*. **(Tab. 5.2)**. Then, a significant anisotropic structural rearrangement takes place with hydration, which is probably due to the formation of hydrogen bonds between neighboring tetrahedra [GaO_4], along a direction nearly parallel to the *a* axis.

Sample	T (°C)	a (Å)	b (Å)	c (Å)	V (Å^3)
LBG0	29	10.0173 ± 3E-4	7.2690 ± 3E-4	5.9121 ± 2E-4	430.50 ± 2E-2
LBG5d	51	10.0272 ± 4E-4	7.2700 ± 4E-4	5.9097 ± 3E-4	430.80 ± 2E-2
LBG10d	31	10.0596 ± 9E-4	7.3071 ± 9E-4	5.9275 ± 8E-4	435.71 ± 6E-2
LBG15d	49	10.0812 ± 8E-4	7.3100 ± 7E-4	5.9255 ± 7E-4	436.67 ± 4E-2
LBG20d	23	10.0931 ± 6E-4	7.3145 ± 6E-4	5.9361 ± 6E-4	438.24 ± 4E-2
Total Increment		0.076	0.046	0.024	7.7
NBG0	36	9.9400 ± 9E-4	7.1349 ± 9E-4	5.8506 ± 8E-4	414.93 ± 6E-2
NGB5d	30	9.9482 ± 8E-4	7.1389 ± 6E-4	5.8478 ± 5E-4	415.30 ± 4E-2

Sample	T (°C)	a (Å)	b (Å)	c (Å)	V (Å^3)
LBG0	29	10.0173 ± 3E-4	7.2690 ± 3E-4	5.9121 ± 2E-4	430.50 ± 2E-2
LBG5	-	-	-	-	-
LBG10	22	10.0443 ± 8E-4	7.3180 ± 7E-4	5.9279 ± 7E-4	435.72 ± 4E-2
LBG15	28	10.0503 ± 6E-4	7.3315 ± 6E-4	5.9310 ± 6E-4	437.02 ± 3E-2
LBG20	25	10.0677 ± 5E-4	7.3510 ± 5E-4	5.9387 ± 5E-4	439.51 ± 3E-2
Total increment		0.050	0.082	0.027	9.0
NBG0	36	9.9400 ± 9E-4	7.1349 ± 9E-4	5.8506 ± 8E-4	414.93 ± 6E-2
NBG5	34	9.9481 ± 7E-4	7.1444 ± 6E-4	5.8519 ± 5E-4	415.92 ± 4E-2

Tab. 5.2. Cell parameters obtained by fitting of XRD data collected at about 30°C. "Total increment" means the overall variation of parameter from LBG0 to LBG20. The cell parameter increases as a function of dopant amount. In wet samples a decrease of the *a* parameter, an increase of *b*, and a smaller increase of *c* can be recognized.

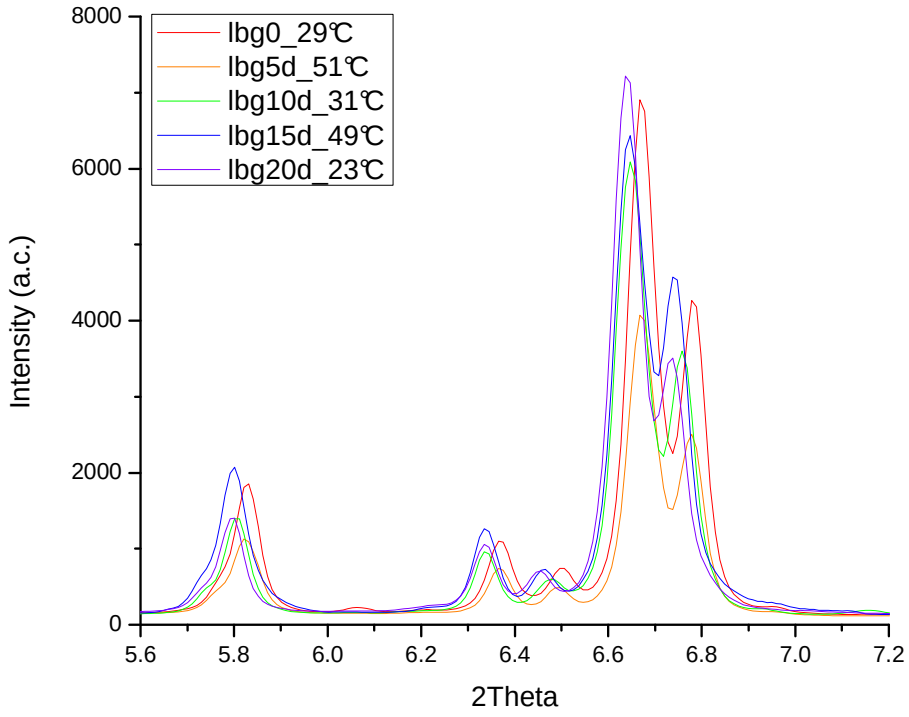

Fig. 5.5. Comparison of some XRD diffraction peaks for dry samples. We can notice a shift of diffraction peaks to smaller angles due to increase of cell parameters as a function of dopant amount.

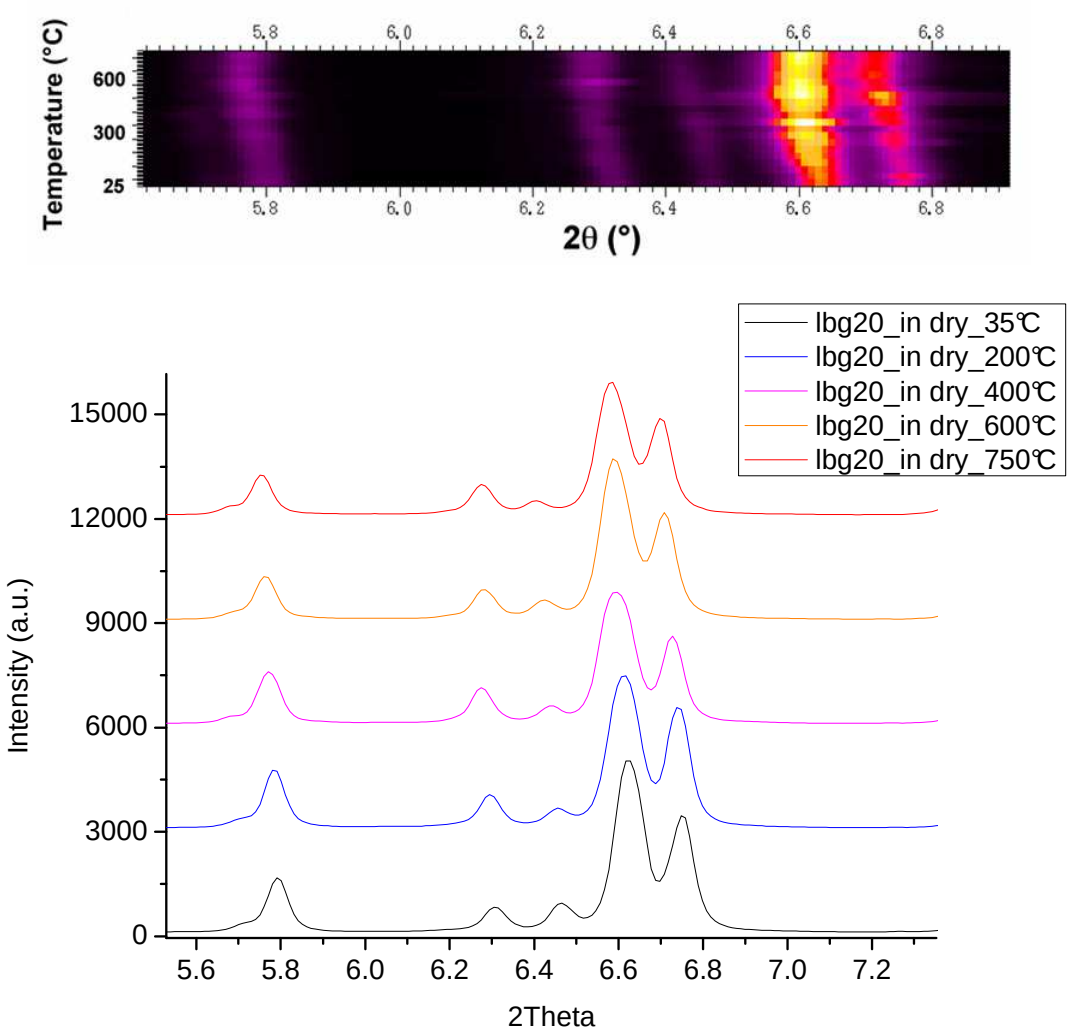

Fig. 5.6. a) *In situ* XRD data of sample LBG20: heating ramp from 25°C to 750°C in dry flux. It is possible to notice the shift of diffraction peaks towards lower angles, due to thermal expansion of the structure. **b)** Diffraction patterns of the same ramp, at different temperatures.

In **fig. 5.6** the *in situ* XRD data of samples LBG20 heating from 25°C to 750°C in dry flux are reported. It is possible to notice the shift of the diffraction peaks towards lower angles, due to thermal expansion of the structure.

For low doping levels (5-10%) the *b* axis linear expansion coefficient in wet samples, calculated from Rietveld refinement, is smaller than in dry samples; by contrast, an opposite behavior can be noticed along the *a* axis **(Tab. 5.3)**. This observation provides further support to the hypothesis of anisotropic formation of hydrogen bonds between neighboring tetrahedra [GaO_4]. For higher doping levels (15-20%) the analysis of thermal expansion is biased by structural disorder.

Sample	α(a)	α(b)	α(c)
LBG5	$1.02*10^{-5} \pm 2*10^{-7}$	$1.12*10^{-5} \pm 2*10^{-7}$	$7.2*10^{-6} \pm 2*10^{-7}$
LBG5d	$7.7*10^{-6} \pm 3*10^{-7}$	$1.57*10^{-5} \pm 8*10^{-7}$	$9.0*10^{-6} \pm 3*10^{-7}$
LBG10	$1.07*10^{-5} \pm 9*10^{-7}$	$1.1*10^{-5} \pm 1*10^{-6}$	$8.9*10^{-6} \pm 5*10^{-7}$
LBG10d	$6.5*10^{-6} \pm 3*10^{-7}$	$1.6*10^{-5} \pm 1*10^{-6}$	$9.7*10^{-6} \pm 7*10^{-7}$

Tab. 5.3. Linear expansion coefficient along the three crystallographic axes, calculated by Rietveld refinement of *in situ* XRD patterns. The coefficient in wet samples is smaller than in dry samples; an opposite behavior can be recognized along the *a* axis.

5.5 EXAFS Analysis

The EXAFS data were collected at the **XAFS** beamline of the **ELETTRA** synchrotron (Trieste) at the Ga K–edge (10.4 KeV) at 77 K. Using the packages Feff6 and Viper, the spectra were modeled with 15 atomic distances; an illustrative example is shown in **Fig. 5.7**. Moreover, in **Fig. 5.8 and 5.9** comparisons between the FT of dry and wet samples, respectively for LBG20 and NBG5 are shown.

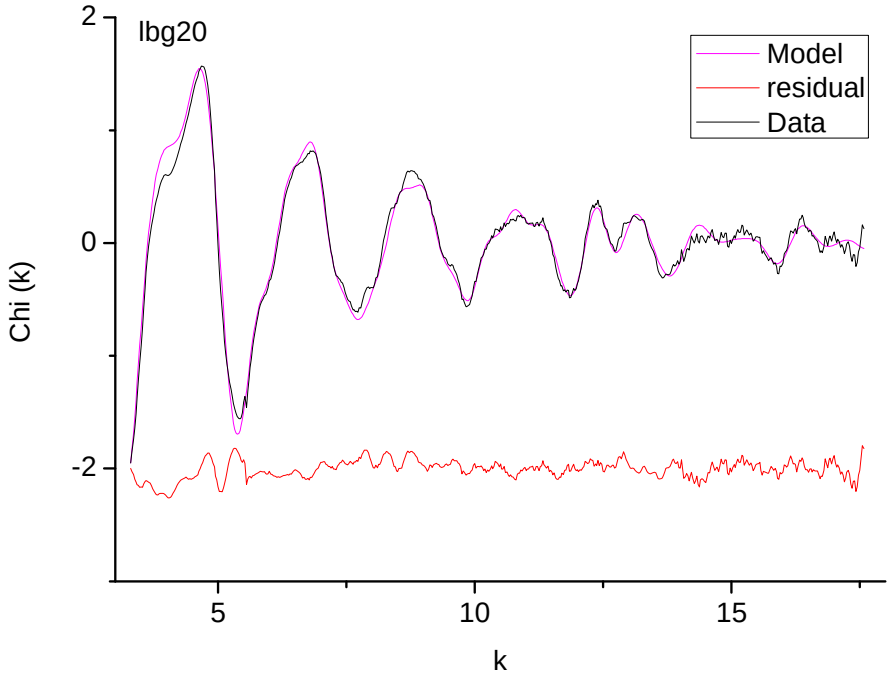

Fig. 5.7. EXAFS data (black line) and model (pink line) of LBG20 sample. The residual (red line) draws the difference between the experimental data and the model signal.

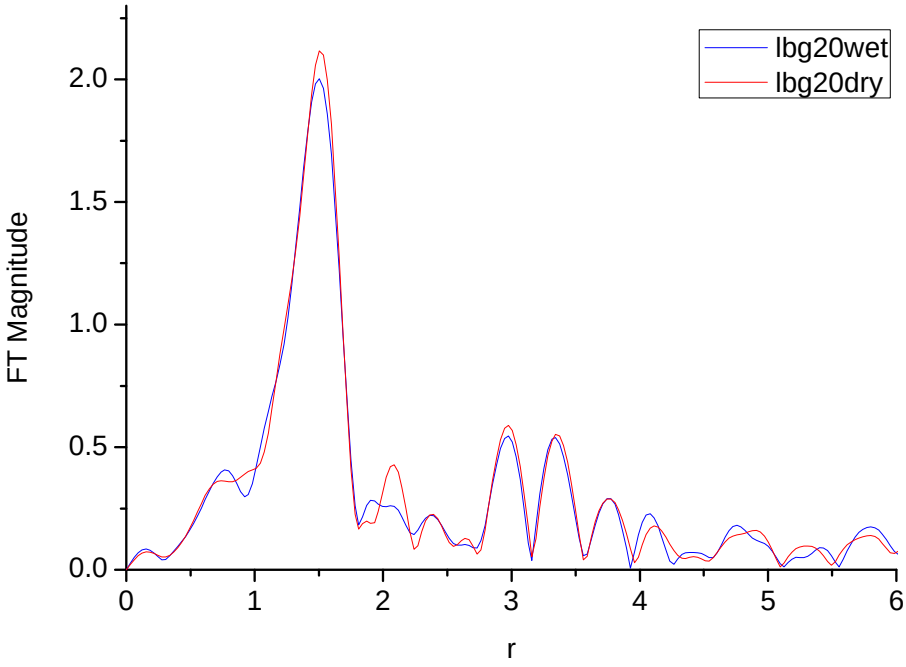

Fig. 5.8. Comparison between the FT data of samples LBG20 (blue line) and LBG20d (red line).

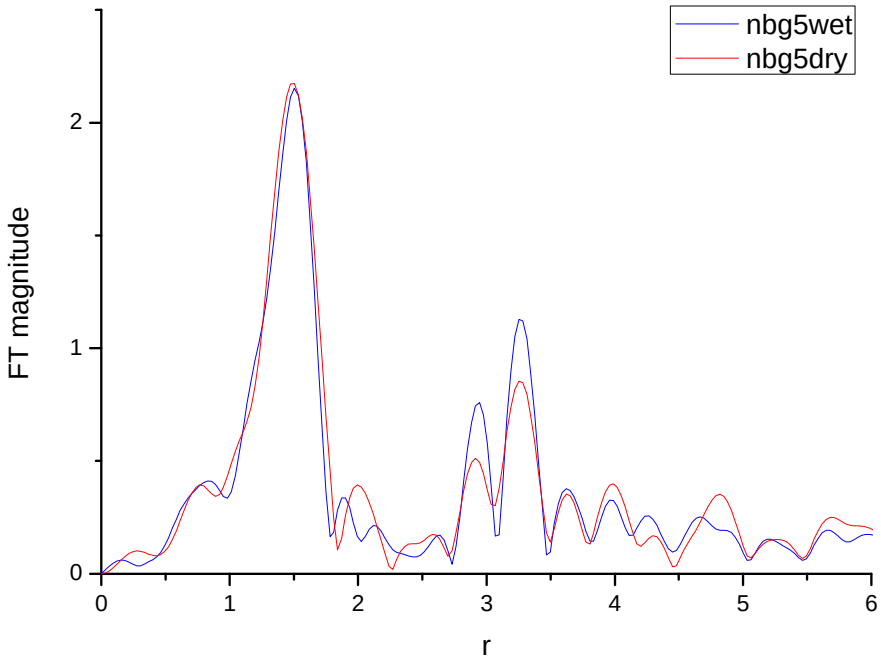

Fig. 5.9. Comparison between the FT data of samples NBG5 (blue line) and NBG5d (red line).

The parameters used for all the EXAFS analyses, namely the 15 atomic distances (plus one of multiple scattering) and the Debye–Waller factors of disorder, are reported in **Tab. 5.4, 5.5 and 5.6**.

In general, for perovskite-type (ABO_3) proton conductors the octahedra [BO_6] are distorted or strained as a function of the dopant amount; therefore the B-O atomic distances and disorder factors change accordingly **[giannici2010]**. Unlike the behavior of proton conducting perovskites, in the investigated $RE_{1-x}Ba_{1+x}GaO_{4-x/2}$ the first-neighbors Ga-O distances do not vary as a function of dopant amount. The disorder factor of the first-neighbor oxygen anions increases slightly in the series of the samples. These results suggest that the [GaO_4] tetrahedra remain essentially unperturbed on increasing the dopant amount. The effect of doping is noticed in the increase of the disorder factors of next-neighboring shells **(Tab. 5.4, 5.5 and 5.6)**. Temperature variation does not cause significant effects in Ga-O first distances as well, so suggesting the rigidity of [GaO_4] tetrahedra **(Fig. 5.10)**. The rigidity of [GaO_4] tetrahedra can explain the high calculated activation energy of intra-tetrahedra proton hopping **[kendrick2007]**.

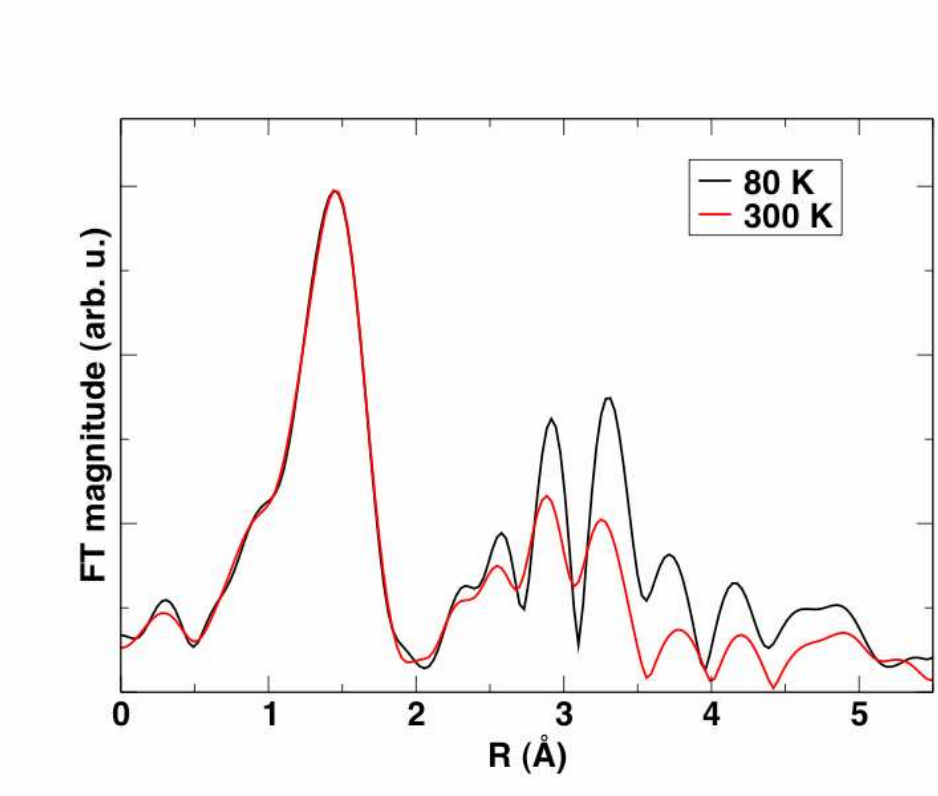

Fig. 5.10. FT - EXAFS data of samples LBG0 at 80 K (black line) and 300 K (red line).

For the LBG20 dry sample, Kendrick et al. proposed the formation of [Ga_2O_7] clusters **[kendrick2007]**. By contrast, the EXAFS analysis shows that in dry samples the average of the first two Ga-Ga distances (at about 4.62 Å and 4.85 Å) has only a slightly decreasing trend in association with the highest doping level (15-20%) **(Fig. 5.11)**. The lack of considerable variations in the Ga-Ga distances between dry and wet samples suggests that the hydroxyl defects involve mostly an orientational rearrangement of [GaO_4] tetrahedra.

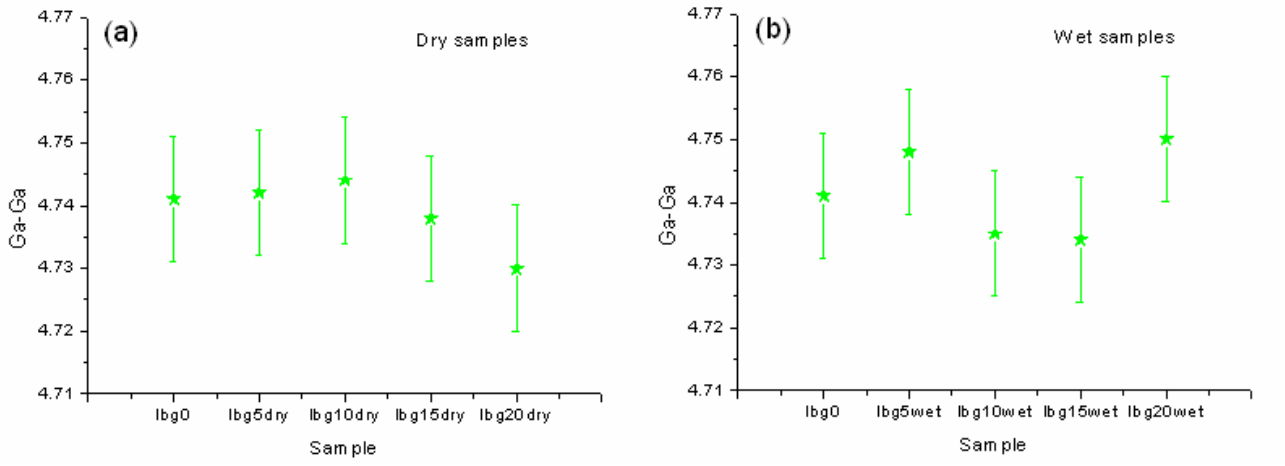

Fig. 5.11. Average of the first two Ga-Ga distances (at about 4.62 Å and 4.85 Å) as a function of the dopant amount in dry **(a)** and wet **(b)** samples. This value has only a slight contraction trend in correspondence of the highest doping level in dry samples.

Distances & Disorder		LBG0	LBG5	LBG10	LBG15	LBG20
R_1	4x Ga-O	1.85	1.85	1.84	1.85	1.85
R_2	1x Ga-O	3.01	3.00	3.00	3.01	3.02
$\sigma^2_{O1,2}$		0.0030	0.0030	0.0031	0.0031	0.0036
R_3	2x Ga-Me	3.25	3.25	3.25	3.25	3.25
σ^2_{Me3}		0.0035	0.0036	0.0035	0.0042	0.0055
R_4	4x Ga-Me	3.43	3.43	3.43	3.44	3.44
σ^2_{Me4}		0.0055	0.0056	0.0053	0.0062	0.0087
R_5	1x Ga-Me	4.05	4.06	4.05	4.07	4.07
R_6	3x Ga-Me	4.19	4.18	4.18	4.18	4.18
R_{6b}	2x Ga-Me-O*	"	"	"	"	"
σ^2_{Me6b}		0.0027	0.0025	0.0026	0.0033	0.0057
R_7	7x Ga-O	4.34	4.33	4.33	4.33	4.32
R_8	1x Ga-Me	4.41	4.36	4.38	4.29	4.29
$\sigma^2_{Me5,6,8}$		0.0060	0.0065	0.0064	0.0071	0.0085
R_9	8x Ga-O	4.72	4.73	4.72	4.72	4.73
R_{10}	2x Ga-Ga	4.63	4.65	4.63	4.64	4.62
R_{11}	2x Ga-Ga	4.85	4.85	4.84	4.83	4.88
R_{12}	4x Ga-O	4.95	4.94	4.95	4.94	4.99
R_{13}	2x Ga-Ga	5.29	5.29	5.27	5.28	5.23
R_{14}	6x Ga-O	5.37	5.37	5.37	5.38	5.38
$\sigma^2_{O7,9,12,14}$		0.0023	0.0026	0.0026	0.0030	0.0045
R_{15}	4x Ga-Ga	5.93	5.93	5.93	5.93	5.93
$\sigma^2_{Ga10,11,13,15}$		0.0067	0.0068	0.0071	0.0082	0.0102

* = Multiple scattering path

Tab. 5.4. EXAFS parameters for wet LBGX samples: 15 atomic distances (plus one multiple scattering path) and the corresponding Debye-Waller factors. The atomic scattering factors of Ba and La are similar, so both were considered the same *Me* atom. The distances are reported in Å and the disorder factors in Å^2.

Distances & Disorder		LBG0	LBG5d	LBG10d	LBG15d	LBG20d
R_1	4x Ga-O	1.85	1.84	1.84	1.84	1.85
R_2	1x Ga-O	3.01	2.98	2.97	3.00	3.02
$\sigma^2_{O1,2}$		0.0030	0.0034	0.0032	0.0043	0.0032
R_3	2x Ga-Me	3.25	3.25	3.25	3.25	3.25
σ^2_{Me3}		0.0035	0.0034	0.0032	0.0064	0.0053
R_4	4x Ga-Me	3.43	3.43	3.43	3.43	3.44
σ^2_{Me4}		0.0055	0.0056	0.0053	0.0096	0.0087
R_5	1x Ga-Me	4.05	4.04	4.05	4.07	4.07
R_6	3x Ga-Me	4.19	4.17	4.18	4.18	4.20
R_{6b}	2x Ga-Me-O*	“	“	“	“	“
σ^2_{Me6b}		0.0027	0.0028	0.0026	0.0062	0.0065
R_7	7x Ga-O	4.34	4.32	4.33	4.32	4.33
R_8	1x Ga-Me	4.41	4.32	4.31	4.27	4.24
$\sigma^2_{Me5,6,8}$		0.0060	0.0063	0.0069	0.0095	0.0120
R_9	8x Ga-O	4.72	4.71	4.70	4.73	4.73
R_{10}	2x Ga-Ga	4.63	4.64	4.66	4.61	4.59
R_{11}	2x Ga-Ga	4.85	4.84	4.83	4.86	4.87
R_{12}	4x Ga-O	4.95	4.95	4.92	4.98	4.99
R_{13}	2x Ga-Ga	5.29	5.27	5.29	5.23	5.24
R_{14}	6x Ga-O	5.37	5.36	5.37	5.36	5.37
$\sigma^2_{O7,9,12,14}$		0.0023	0.0025	0.0024	0.0048	0.0052
R_{15}	4x Ga-Ga	5.93	5.92	5.93	5.92	5.91
$\sigma^2_{Ga10,11,13,15}$		0.0067	0.0073	0.0075	0.0109	0.0107

* = Multiple scattering path

Tab. 5.5. EXAFS parameters for dry LBGX samples: 15 atomic distances (plus one multiple scattering path) and the corresponding Debye-Waller factors. The atomic scattering factors of Ba and La are similar, so both were considered the same *Me* atom. The distances are reported in Å and the disorder factors in $Å^2$.

Distances & Disorder		NBG0	NBG5	NBG5d
R_1	4x Ga-O	1.85	1.85	1.86
R_2	1x Ga-O	2.99	2.97	2.96
$\sigma^2_{O1,2}$		0.0029	0.0032	0.0034
R_3	2x Ga-Me	3.25	3.24	3.25
σ^2_{Me3}		0.0030	0.0035	0.0046
R_4	4x Ga-Me	3.40	3.39	3.39
σ^2_{Me4}		0.0032	0.0042	0.0050
R_5	1x Ga-Me	3.55	3.55	3.53
R_6	3x Ga-Me	4.11	4.11	4.12
R_{6b}	2x Ga-Me-O*	"	"	"
σ^2_{Me6b}		0.0028	0.0042	0.0046
R_7	7x Ga-O	4.23	4.22	4.24
R_8	1x Ga-Me	4.36	4.34	4.21
$\sigma^2_{Me5,6,8}$		0.0062	0.0065	0.0058
R_9	8x Ga-O	4.66	4.65	4.70
R_{10}	2x Ga-Ga	4.55	4.54	4.57
R_{11}	2x Ga-Ga	4.84	4.82	4.88
R_{12}	4x Ga-O	4.93	4.92	5.00
R_{13}	2x Ga-Ga	5.26	5.26	5.27
R_{14}	6x Ga-O	5.63	5.65	5.71
$\sigma^2_{O7,9,12,14}$		0.0031	0.0041	0.0040
R_{15}	4x Ga-Ga	5.85	5.86	5.90
$\sigma^2_{Ga10,11,13,15}$		0.0068	0.0075	0.0061

* = Multiple Scattering path

Tab. 5.6. EXAFS parameters for dry NBGX samples: 15 atomic distances (plus one multiple scattering path) and the corresponding Debye-Waller factors. The atomic scattering factors of Ba and Nd are similar, so both were considered the same *Me* atom. The distances are reported in Å and the disorder factors in $Å^2$.

5.6 HR-XRD Analysis

High-resolution XRD data were collected at the **ID31** beamline of **ESRF** synchrotron (Grenoble) using a λ= 0.4 Å radiation. All the data were collected at room temperature. The diffracted radiation was collected by a bank of eight Si(111) analyzer crystals. The GSAS package was used to fit the diffraction patterns. At first, unconstrained fittings were performed using the orthorhombic $P2_12_12_1$ space group **[rüter1990]**. A representative result, relative to the LBG20 sample, is reported in **Fig. 5.12**.

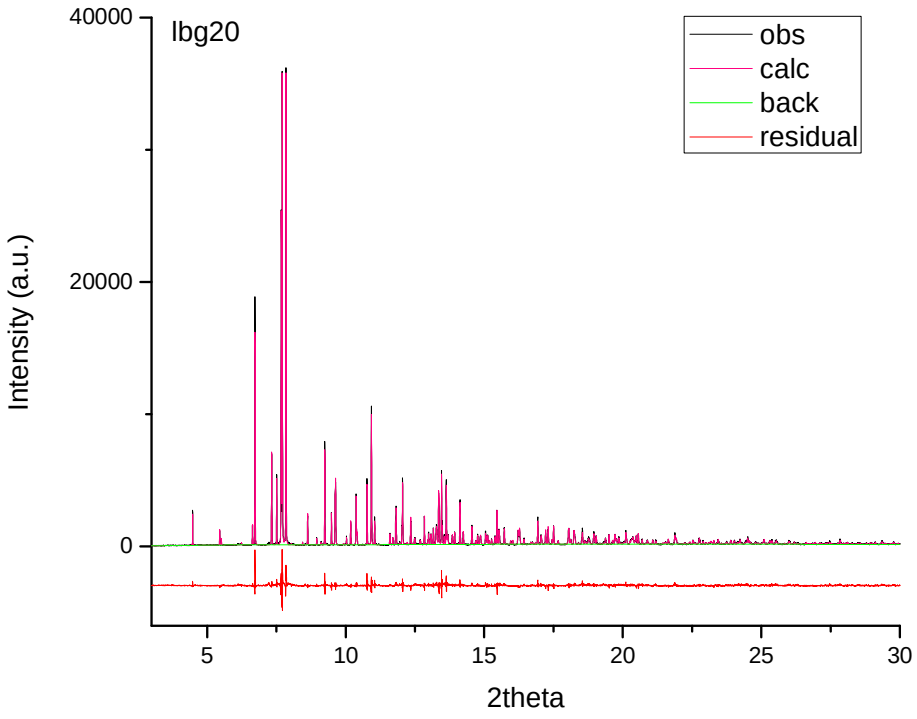

Fig. 5.12. XRD data (black line) and model (pink line) of LBG20 sample. The residual (red line) is drawn.

On the basis of the EXAFS data, that led to consider the [GaO_4] tetrahedra as rigid bodies, constrained fitting runs were also tried: using the atomic positions of LBG0, it was carried out a **rigid body fitting run** of LBG20d and LBG20 in which all distances and angles of the **[GaO_4]** tetrahedron did not vary. According to these analyses, the structural rearrangement from dry to wet structures consists essentially in a slight rotation of the rigid [GaO_4] tetrahedra that leaves almost unchanged the Ga-Ga distances between the Ga centers of neighboring tetrahedra. The use of constraints between the fitting parameters involved an only slight worsening of the goodness of fit. However, the results given from this approach were unsatisfactory from the point of view of interpretation, mostly because a very small difference in the inter-tetrahedra oxygen distances of LBG20 and LBG20d is determined,

with an essentially random variation of O-O inter-tetrahedral distances between the dry and wet sample.

The unconstrained Rietveld analysis confirms that the dopant insertion causes an increase in the cell parameters, in particular the increase along *a* is larger than the other two. Obviously, the formation of oxygen vacancies causes an increase of the disorder factors, in particular the one pertaining to the oxygen anions **(Tab. 5.7)**. In agreement with the *in situ* – XRD analysis, hydration mostly produces a decrease of the *a* parameter, pointing to the formation of hydrogen bonds between neighboring tetrahedra [GaO_4] along a direction approximately parallel to the *a* axis. Moreover, hydration involves the filling of oxygen vacancies with hydroxyl defects, and a consequent decrease of the oxygen disorder factors. The parallel decrease of σ^2_{Ga} , definitely larger than the La/Ba disorder factor, could be related to the formation of inter-tetrahedral hydrogen bonds, involving a rearrangement of the network of [GaO_4] tetrahedra **(Tab. 5.7)**.

	LBG0	LBG20d	LBG20
a (Å)	10.01502 ± 5E-5	10.09987 ± 5E-5	10.07355 ± 4E-5
b (Å)	7.26659 ± 5E-5	7.31373 ± 3E-5	7.35508 ± 4E-5
c (Å)	5.91073 ± 3E-5	5.93557 ± 3E-5	5.94534 ± 2E-5
V (Å^3)	430.154 ± 3E-3	438.447 ± 3E-3	440.501 ± 2E-3
σ^2_{Me} (Å^2)	0.0135 ± 2E-4	0.0245 ± 2E-4	0.0206 ± 2E-4
σ^2_{Ga} (Å^2)	0.0105 ± 6E-4	0.0184 ± 6E-4	0.0117 ± 4E-4
σ^2_{O} (Å^2)	0.016 ± 2E-3	0.053 ± 2E-3	0.039 ± 2E-3

Tab. 5.7. Cell parameters and Debye-Waller factors. Values obtained by fitting of HR-XRD data. The DB factors were assumed to be the same for all the oxygens (σ^2_O) and for lantanum and barium (σ^2_{Me}).

The HR-XRD data were collected at room temperature. At this temperature no significant proton conduction occurs. Therefore, the refinement of atomic positions suggests the picture of a material in which it is possible to identify the “frozen” position of protons **(Fig. 5.13)**.

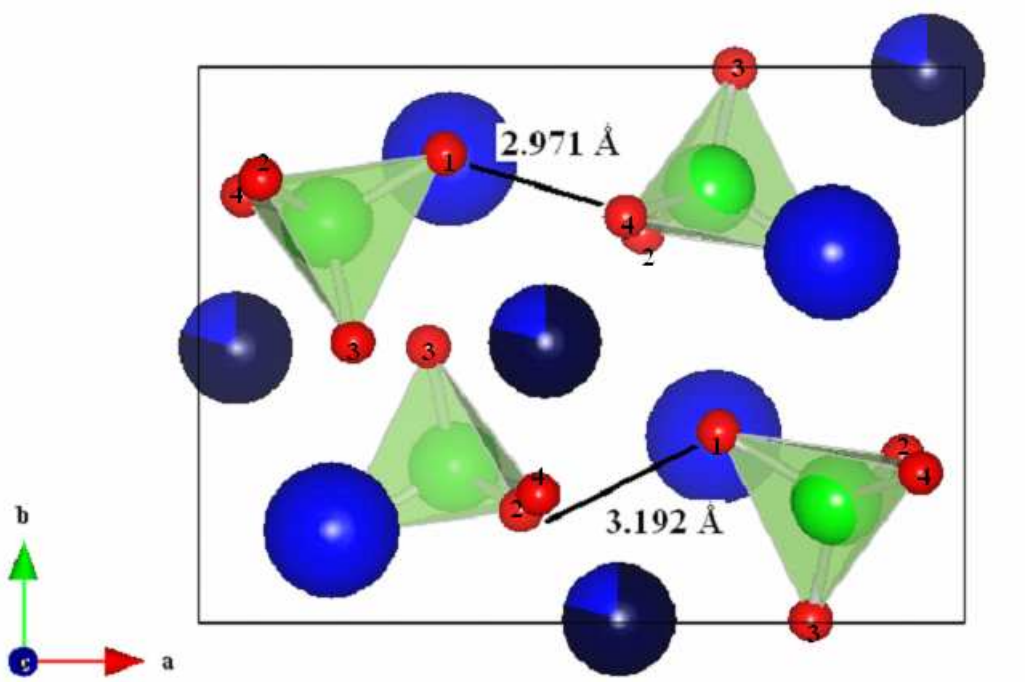

Fig. 5.13: Structure of LBG20 drawn by the VESTA program from HD-XRD data. The Ga^{3+} cations (green balls) reside in the tetrahedra of oxygen anions (red balls). (La^{3+} - deep blue balls; Ba^{2+} - light blue balls). The shortest distances inter-tetrahedra (O_1-O_4), and the distances O_1-O_2 are emphasized.

Hydration causes a slight rotation of tetrahedra and a rearrangement of atomic distances: the inter-tetrahedra distance O_1 - O_4, which is almost parallel to the *a* axis, becomes shorter, passing from 3.051 Å to 2.971 Å. Noticeably, no other inter-tetrahedra distances become so much shorter **(Tab. 5.8 and Fig. 5.13)**. Most likely, protons are located in the interstitial O_1 – O_4 region, in agreement with the theoretical simulations of Kendrick et al. **[kendrick2007]**. Correspondingly, the Ga-O_4 intra-tetrahedral bond is stretched from 1.770 Å to 1.875 Å **(Tab. 5.9)**.

Sample	d(O_1-O_4) (Å)	d(O_1-O_2) (Å)
LBG0	3.045	3.002
LBG20d	3.051	3.090
LBG20	2.971	3.192

Tab. 5.8. The shortest inter-tetrahedral (O_1-O_4) distances and the O_1-O_2 distances are reported for all the analyzed samples. Distances calculated from the HD-XRD data.

Distances (Å)	LBG0	LBG20d	LBG20
Ga-O_1	1.850	1.815	1.806
Ga-O_2	1.861	1.886	1.739
Ga-O_3	1.832	1.749	1.773
Ga-O_4	1.803	1.770	1.875
Average	1.836	1.805	1.798

Tab. 5.9. The first four Ga-O distances and their average. The distances are calculated from the HD-XRD data.

5.7 EIS Analysis

EIS data were collected at Dipartimento di Scienze e Tecnologie Chimiche of the University of Roma "Tor Vergata" using a Multichannel Potentiostat VMP3 (Princeton Applied Research). Impedances were measured in the frequency range of 500k Hz-0.1 Hz at temperatures generally ranging from 400 °C to 700 °C, and under different dry or wet atmospheres, namely of hydrogen, synthetic air and argon. Each set of measures were modeled with an equivalent circuit using the ZSimpWin software; two illustrative examples are reported hereafter **(Fig 5.14 – 5.15)**.

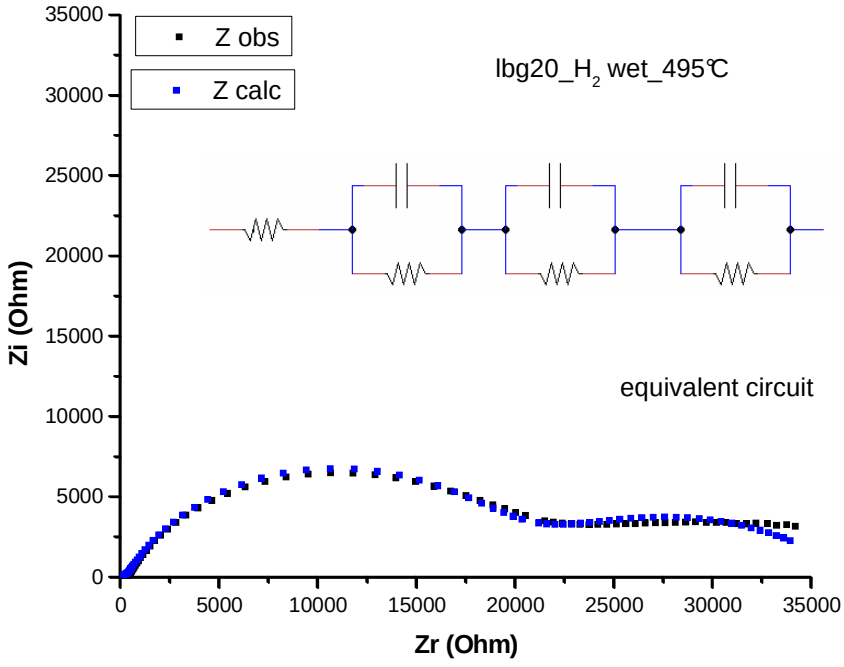

Fig. 5.14. EIS data (black squares) and model (blue squares) of LBG20 sample. Data measured at 495°C in H_2 wet atmosphere. The picture shows also the equivalent circuit used to model the data.

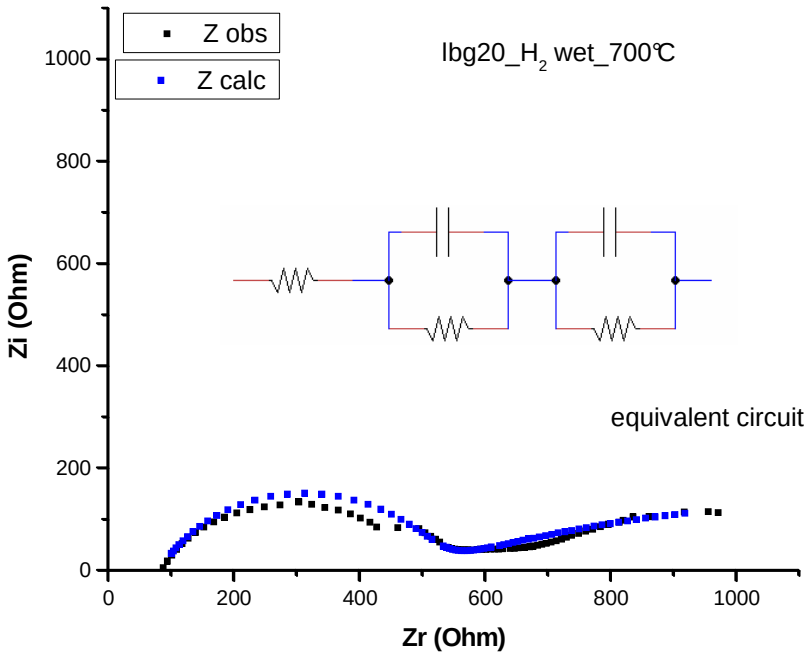

Fig. 5.15. EIS data (black squares) and model (blue squares) of LBG20 sample. Data measured at 700°C in H_2 wet atmosphere. The picture shows also the equivalent circuit used to modeling the data.

The conductivity of the bulk material in wet atmosphere is much higher than in dry gas flux **(Fig. 5.16a)**, as expected assuming that proton conduction takes place in these materials. This difference in conductivity decreases at the highest temperatures according to decrease of mole fraction of water incorporated into the structure **(Fig. 5.17)**. By contrast, the grain boundary conductivities in wet and dry atmosphere are similar. Consequently, it can be concluded that the proton mobility at the grain boundary region is very low **(Fig. 5.16b)**. The same drawback is present in $BaZrO_3$ -based proton conductors, where the formation of grain boundary minor phases was proposed as a probable cause of the decreased proton mobility in that region **[kreuer2003].**

In a semiconductor the conductivity decreases under reducing conditions, depending on $p(O_2)^{-1/4}$, if the semiconductor is *n*-type; differently, it increases under oxidizing conditions, depending on $p(O_2)^{+1/4}$, if the semiconductor is *p*-type **[haugsrud2006b]**. In all the studied samples the bulk conductivity is higher in dry air than in dry argon; therefore, it is possible that *p*-type electronic conduction takes place in dry atmospheres **(Fig. 5.16a)**.

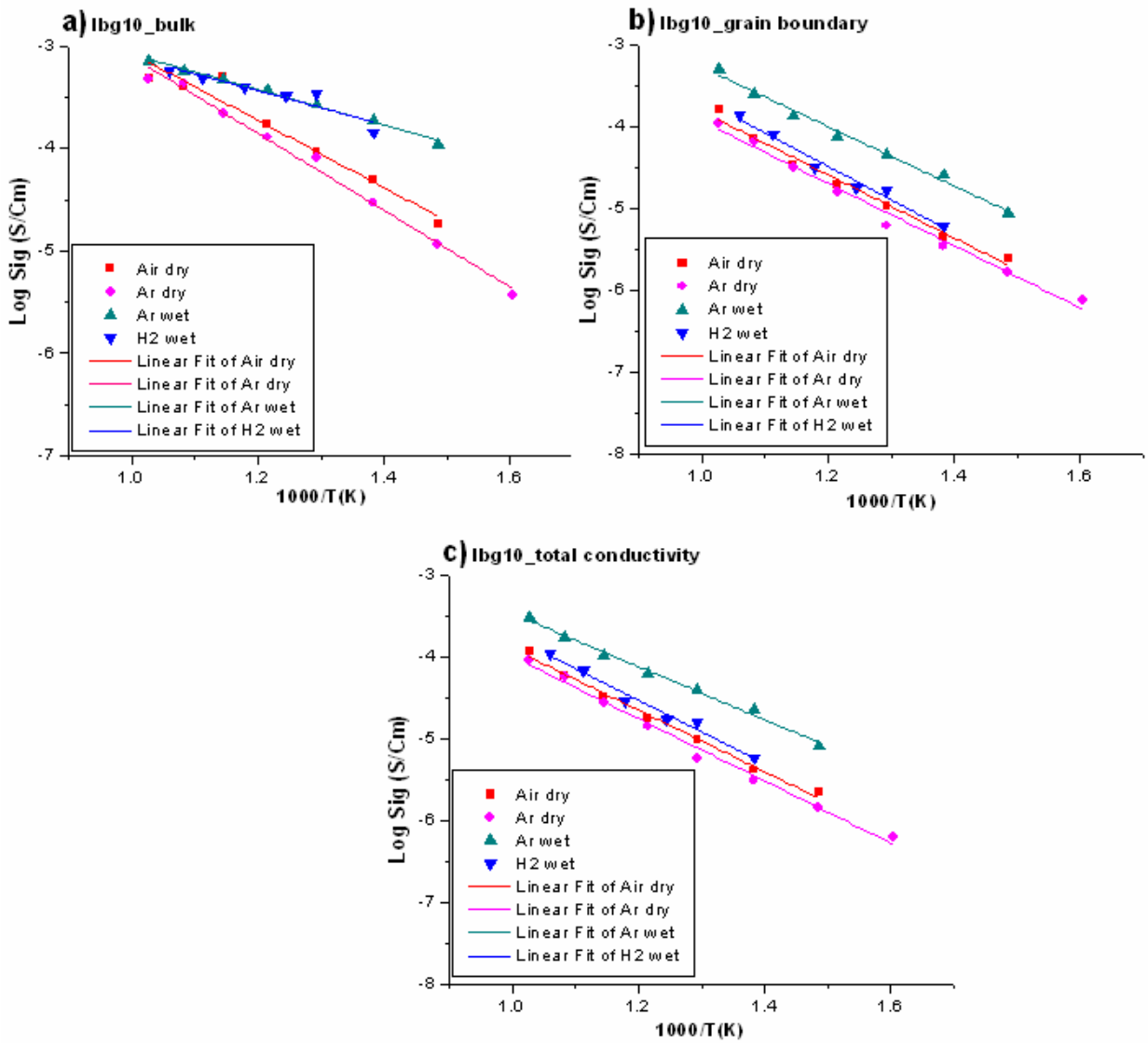

Fig. 5.16. Arrhenius plots of LBG10 sample in H_2 and Ar "wet", Ar and Air "dry" atmospheres: **a)** bulk conductivity; **b)** grain boundary conductivity; **c)** total conductivity.

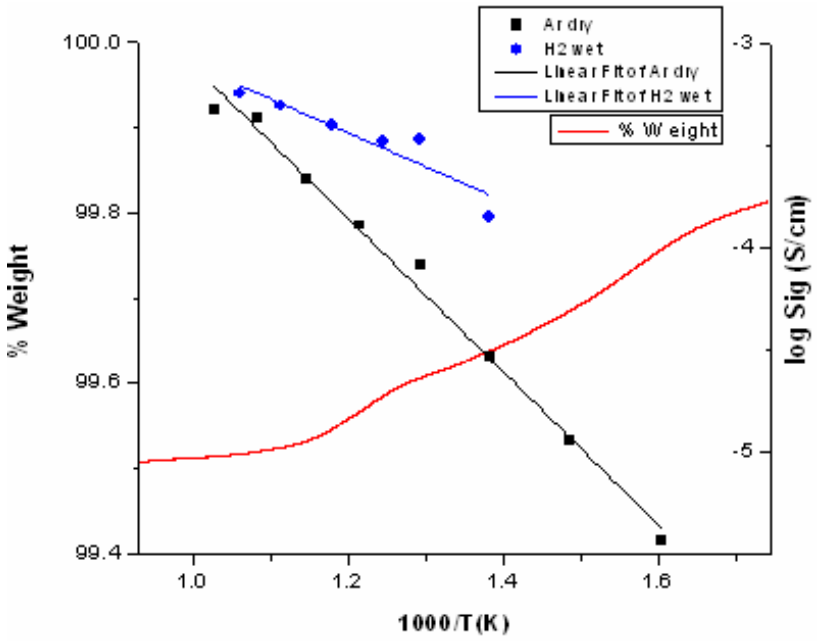

Fig. 5.17. Comparison between Arrhenius plots of bulk conductivity in H2 "wet" and Ar "dry", and TGA curve of LBG10 sample in the same range of temperatures.

The bulk conductivities in wet Ar and H_2 show the same features, but the grain boundary conductivity is higher in Ar than in H_2 wet atmosphere. Further experiments are planned to confirm this behavior.

The reduced grain boundary conductivity could be due, as in barium zirconate materials, to a demixing of minor phases, such as BaO. An evidence of such minor phases formation is given by XPS (X-ray Photoelectron Spectroscopy) data (collected at ISMN-CNR of Palermo). These data, reported in the **tab. 5.10**, show that in the sample surface there is a larger content of lanthanum and barium than of gallium, in contrast with the stoichiometric composition of material.

Element	**at %**
O	81.0
C	55.0 (probably CO_2)
Ba	6.8
La	8.2
Ga	4.0

Tab. 5.11. Rate of elements at the surface of LBG0 sample given by XPS technique.

The highest conductivity of the bulk takes place in the sample having the biggest amount of dopant; on the other hand, the grain boundary conductivity is independent of dopant amount

(Fig. 5.18a). The LBG20 sample has a total proton conductivity of $1.4*10^{-4}$ S/Cm at 700°C in H_2 wet atmosphere. **(Tab. 5.11)**.

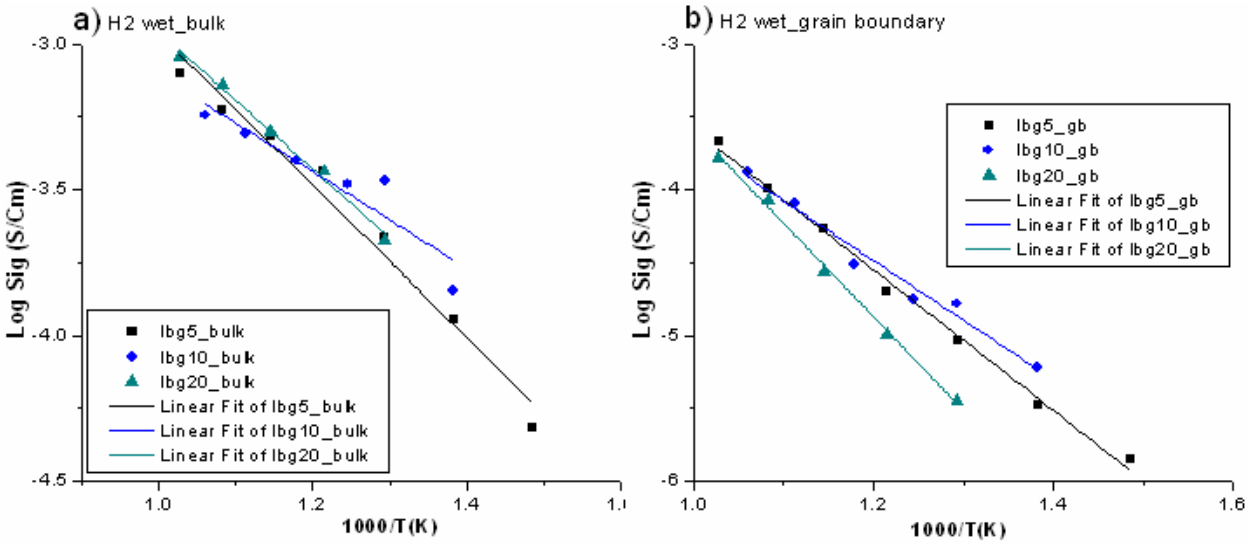

Fig. 5.18. Comparison of Arrhenius plots in H_2 wet atmospheres. **a)** bulk conductivity **b)** grain boundary conductivity.

Sample		Conductivity (S/Cm)	Temperature (°C)	Atmosphere
LBG20	Bulk	$9.0\ 10^{-4}$	700	H_2 wet
	GrainBoundary	$1.6\ 10^{-4}$	700	H_2 wet
	Total	$1.4\ 10^{-4}$	700	H_2 wet
	Bulk	$5.9\ 10^{-4}$	700	Ar dry
	GrainBoundary	$9.5\ 10^{-5}$	700	Air dry
	Total	$7.9\ 10^{-5}$	700	Air dry

Tab. 5.11. Highest conductivity values measured for LBG20 sample in dry and wet atmospheres.

A comparison between the conductivities of samples LBG5 and NBG5, differing for the rare earth cations, shows that the conductivity of bulk is higher in the former one, whereas the conductivity of grain boundary is higher in the latter sample at lower temperatures **(Fig. 5.19)**.

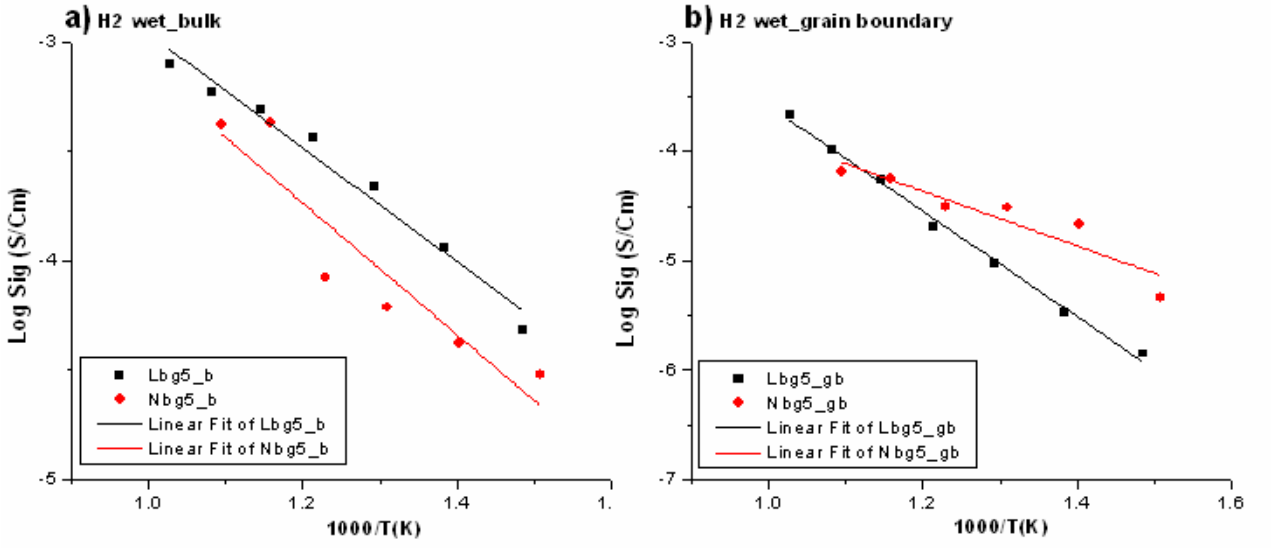

Fig. 5.19. Arrhenius plots comparison in H_2 wet atmospheres of samples LBG5 (black points) and NBG5 (red points). **a)** bulk conductivity **b)** grain boundary conductivity.

5.8 Conclusions

The new-generation **$RE_{1-x}Ba_{1+x}GaO_{4-x/2}$ (RE = La, Nd)** proton conductor oxides were investigated with several synchrotron radiation techniques (***in situ* – XRD, HR-XRD, EXAFS**) and with **TGA** and **EIS**. The combined informations obtained by these different techniques allowed to draw an overall picture of the structure of these materials and to outline a reliable relationship of the structural features with proton conduction:

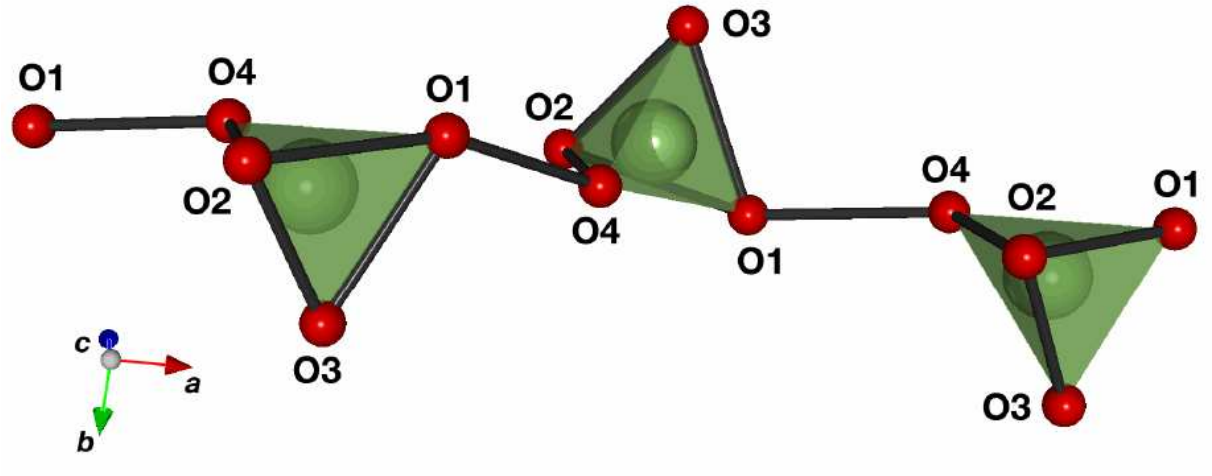

Fig. 5.20. Fragment of the crystal structure of LBG20. The La and Ba atoms are removed for clarity, Ga atoms are drown in green and the O atoms in red. Only O-O distances shorter than 3 Å are shown as solid lines.

- Powders with a single orthorhombic phase can be prepared in the range of composition: LBGx, $0 \leq x \leq 0.2$ and NBGx, $0 \leq x \leq 0.05$. All samples are able to give rise to dissociative incorporation of water as a function of self-doping amount.
- The [GaO_4] tetrahedra remain essentially rigid on increasing the dopant amount, after hydration and also by increasing the temperature. The effect of doping is noticed in the increase in the disorder factors of next-neighboring shells. The rigidity of [GaO_4] tetrahedra can explain the high calculated activation energy of intra-tetrahedra proton hopping.
- The EXAFS data do not show any formation of [Ga_2O_7] dimers in dry samples.
- Oxygen vacancy formation and hydration give both rise a significant anisotropic structural rearrangement. The self-doping causes an increase of cell parameters; in particular, the increase along *a* is larger than along the *b* and *c* axes. Hydration causes a decrease of the *a* parameter, an increase of *b* and a smaller increase of *c* parameter; then, it is likely that at room temperature hydrogen bonds are established between neighboring [GaO_4] tetrahedra along a direction approximately parallel to the *a* axis.

- Hydration gives rise to a slight rotation of tetrahedra and to a rearrangement of atomic distances. In particular, the inter-tetrahedral O_1-O_4 distance, which is almost parallel to the *a* axis, is contracted (2.971 Å) and this is the only inter-tetrahedral distance becoming shorter than 3 Å after hydration **(Fig 5.20)**. In correspondence with the formation of the O_1-O_4 inter-tetrahedral distance, the GaO_4 intra-tetrahedral bond is stretched.
- The formation of hydrogen bonds is confirmed by the high negative hydration entropy (ΔS^0 = -118 J/mol) and by the greater decrease in the disorder factor of Ga cations in HR-XRD analysis.
- The LBG20 sample has a total proton conductivity of $1.4*10^{-4}$ S/Cm at 700°C in H_2 wet atmosphere.
- Significant bulk proton conduction takes place in $RE_{1-x}Ba_{1+x}GaO_{4-x/2}$ materials; the highest bulk conductivity was noticed in the sample having the largest dopant amount.
- The values of bulk proton conductivity are lower than in perovskites oxides probably due to the high energy barrier of intra-tetrahedra proton hopping, arising from the rigidity of GaO_4 tetrahedra.
- The grain boundary proton mobility is very low. It is argued that the BaO demixes at the grain boundary during pellet formation and that this secondary phase could affect the grain boundary conductivity.
- The isotropy of migration paths of protons is also limited by the low symmetry of proton environment in these materials.
- The NBG5 sample (studied for the first time) shows the same structural behavior.
  It holds water up to higher temperature than other ones. NBG5 has a lower proton conductivity of bulk and a higher proton conductivity of grain boundary than LBG5 sample.

References

[arachi1999] Y. Arachi, H. Sakai, O. Yamamoto, Y. Takeda, N. Imanishi, Solid State Ionics 121 (1999) 133

[artioli2003] Società Italiana di Fisica - Conference Proceedings vol. 82. Synchrotron Radiation: Fundamentals, Methodologies and Applications (2003), S. Mobilio and G. Vlaic eds. G. Artioli, "Synchrotron X-ray powder diffraction", p. 377-399.

[brown2001] M. E. Brown, Introduction to Thermal Analysis, ed. Kluwer Academic (2001)

[cook1992] R. Cook, J.J. Osborne, J.H. White, R.G. MacDuff, A.F. Sammells, J. Electrochem. Soc. 129 (1992) L19

[ESRF] www.esrf.eu

[fabbri2008] E. Fabbri, A. D'Epifanio, E. Di Bartolomeo, S. Licoccia, E. Traversa, Solid State Ionics 179 (2008) 558-564

[fornasini2003] Società Italiana di Fisica - Conference Proceedings vol. 82. Synchrotron Radiation: Fundamentals, Methodologies and Applications (2003), S. Mobilio and G. Vlaic eds. P. Fornasini, "Introduction to X-ray absorption spectroscopy", p. 129-169.

[giannici2007a] F. Giannici, A. Longo, A. Balerna, K.D. Kreuer, A. Martorana, Chem. Mater. (2007)

[giannici2007b] F.Giannici, A. Longo, F. Deganello, A. Balerna, A. S. Arico, A. Martorana, Solid State Ionics 178 (2007) 587-591

[giannici2010] F. Giannici, A. Longo, K. D. Kreuer, A. Balerna, A. Martorana, Solid State Ionics 181 (2010) 122-125

[grove1839] W.R. Grove, Philos. Mag. 14 (1839) 127

[haile2003] S.M. Haile, Acta Mater. 51 (2003) 5981-6000

[haugsrud2006a] R. Haugsrud, T. Norby, Nat. Mater. 5 (2006) 193-196

[haugsrud2006b] R. Haugsrud, T. Norby, Solid State Ionics 177 (2006) 1129-1135

[haugsrud2007] R. Haugsrud, T. Norby, J. Am. Ceram. Soc. 90 (2007) 1116-1121

[irvine1990] T. S. Irvine, D. C. Sinclair, A. R. West, Adv. Mater. (1990) 132-138

[ishiara1994] T. Ishiara, H. Matuda, Y. Tacita, J. Am. Chem. Soc. 116 (1994) 3801

[iwahara1981] H. Iwahara, T. Esaka, H. Uchida, N. Maeda, Solid State Ionics 3-4 (1981) 359-364

[iwahara1988] H. Iwahara, H. Uchida, K. Ono, K. Ogaki, J. Electrochem. Soc 135 (1988) 529-533

[katahira2000] K. Katahira, Y. Kohchi, T. Shimura, H. Iwahara, Solid State Ionics 138 (2000) 91-98

[kendrick2007] E. Kendrick, J. Kendrick, K. S. Knight, M. S. Islam, P. R. Slater, Nat. Mat. 6 (2007) 871-875

[klementev2001] K. V. Klementev, J. Phys. D 34 (2001) 209-217

[kreuer1999] K.D. Kreuer, Solid State Ionics 125 (1999) 285-302

[kreuer2000] K.D. Kreuer, Solid State Ionics 136-137 (2000) 149-160

[kreuer2003] K.D. Kreuer, Ann. Rev. Mater. Res. 33 (2003) 333-359

[larminie,dicks2003] J. Larmine, A. Dicks, Fuel Cell Systems Explained, ed. Wiley (2003)

[li2003] S. Li, F. Schöngerger, P. R. Slater, Chem. Commun. (2003) 2694-2695

[macdonald,johnson2005] J. R. Macdonald, W. B. Johonson, Impedance Spectroscopy, ed. Wiley-Interscience (2005) 1-26

[malavasi2009] L. Malavasi, C. Ritter, G. Chiodelli, J. Alloy. Compd. 475 (2008) 42-45

[margaritondo2001] G. Margaritondo, J. Alloy. Compd. 328 (2001) 35-41

[margaritondo2003] G. Margaritondo, Y. Hwu, G. Tromba, Conference Proceedings 82– Synchrotron Radiation: Fundamentals, Methodologies and Applications, ed. S. Mobilio and G. Vlaic (2003) 25-53

[mokkelbost2007] T. Mokkelbost, Ø. Andersen, R. A. Strøm, K. Wiik, T. Grande, M.A. Einarsrud, J. Am. Ceram. Soc. 90 (2007) 3395-3400

[mokkelbost2008] T. Mokkelbost, I. Kaus, R. Haugsrud, T. Norby, T. Grande, M.A. Einarsrud, J. Am. Ceram. Soc. 91 (2008) 879-886

[nernst1899] W. Nernst, Z. Elektrochem. 43 (1899) 727

[norby1999] T. Norby, Solid State Ionics 125 (1999) 1-11

[norby2004] T. Norby, M. Widrøe, R. Glöckner, Y. Larring, Dalton T. (2004) 3012-3018

[potter2006] A.R. Potter, R.T. Baker, Solid State Ionics 177 (2006) 1917-1924

[rüter1990] I. Rüter, H. Müller-Buschbaum, Z. Anorg. Allg. Chem. 584 (1990) 119-124

[schönberger2005] F. Schönberger, E. Kendrick, M. S. Islam, P. R. Slater, Solid State Ionics 176 (2005) 2951-2953

[singhal2002] SC. Singhal, Solid State Ionics 138 (2002) 152-153

[solarserver] www.solarserver.de

[steel2001] B.C.H. Steel, A. Heinzel , Nature 414 (2001) 345-352

[toby2001] B. H. Toby, J. Appl. Crystallogr. 34 (2001) 210-213

[tuller1979] H.L. Tuller, A.S. Nowick, J. Electrochem. Soc. 126 (1979) 209

[van berkel1995] F.P.F. van Berkel, G.M. Christine, F.H. van Heuveln, J.P.F. Huijsmans, in: M. Dokiya, O. Yamamoto, H.Togawa, S.C. Singhal (eds), Electrochem. Soc. (1995) 1062

[viterbo2003] Società Italiana di Fisica - Conference Proceedings vol. 82. Synchrotron Radiation: Fundamentals, Methodologies and Applications (2003), S. Mobilio and G. Vlaic eds. D. Viterbo, "Diffraction by crystalline materials and its use with synchrotron radiation", p. 345-376.

[yamamoto2000] O. Yamamoto, Electrochim. Acta 45 (2000) 2423-2435

Acknowledgements

- My warmest thanks to **Prof. Antonino Martorana** who deserves all my esteem for supporting me with precious teachings and advices in these years of hard work. I thank him for giving me the opportunity of such an instructive experience and for the opportunity of working at the ESRF and ELETTRA synchrotrons. I thank him for being Master, captain and a little bit father too, for improving me in the field of the scientific research… Thanks!
- I thank with love my family (**father Antonino, mother Simonetta, Alessandra e Chiara)** for the confidences least placed in me. I thank them for supporting my dreams, even economically, in a society who tends to steal youth's future. Thanks!
- I thank with love the sweet **Simona**. I thank her being close to me with love and helping me in the most difficult moments. (Kiss!)
- I thank heartily **Prof. Paolo Lo Meo**, a friend who tried to guide my, at time, rebel spirit in the "wild jungle" of the University.
- I thank **Dott. Alessandro Longo** and **Dott. Francesco Giannici** for their contribution to this research. I thank Alessandro for his professional advices too.
- I thank **ESRF** (Grenoble) ed **ELETTRA** (Trieste) for the beam-time allowed me at the respective synchrotrons.
- I thank **Prof. Giulio Deganello** for giving me the important opportunity of working at the **ISMN-CNR** of Palermo.
- I thank **Dott. Annamaria Venezia** for the XPS measurements and data analysis.
- I thank **Francesco Giordano** for being helpful during my work days at the ISMN-CNR of Palermo.
- I thank **Prof. Silvia Licoccia** for giving me the important opportunity of working at the **Dipartimento di Scienze e Tecnologie Chimiche of Università di Roma Tor Vergata**.
- I thank **Dott. Elisabetta Di Bartolomeo**, **Dott. Alessandra D'Epifanio**, and **Chiara Pugnalini** for the contribution in the conductivity data collection, I thank you for the professional advices too.
- I thank sincerely **Igor Luisetto** for always being helpful in the days of work at University of Roma Tor Vergata. Such a precious help in "the away match".
- I thank **Prof. Gilberto Vlaic** and **Prof. Settimio Mobilio** for giving me the opportunity of attending the international school of **"X School on Synchrotron**

Radiation 2009”, excellently organized by **Società Italiana di Luce di Sincrotrone** and Synchrotron **ELETTRA** (Duino, September 2009).

- Also thanks to **Veronica**.

Thanks.

- Ringrazio con affetto e stima il **Prof. Antonino Martorana** per avermi seguito in questi anni di duro lavoro con preziosissimi insegnamenti e consigli. Lo ringrazio per avermi dato l’opportunità di questa importante esperienza formativa e per avermi dato l’opportunità di lavorare presso i sincrotroni ESRF ed ELETTRA. Per essere stato Maestro, capitano e anche un po’ padre, per avermi forgiato ed affinato nell’ambito della ricerca scientifica… Grazie!
- Ringrazio con amore la mia famiglia (**papà Antonino, mamma Simonetta, Alessandra e Chiara**) per la fiducia e l’importante appoggio che mi hanno sempre dato. Li ringrazio per aver sostenuto, anche economicamente, i miei sogni, in una società che tende a rubare il futuro ai giovani. Grazie!
- Ringrazio con amore la dolce **Simona**. La ringrazio per essermi stata vicino con amore ed avermi aiutato nei momenti più difficili. (Bacio).
- Ringrazio con affetto il **Prof. Paolo Lo Meo**, un amico che ha cercato di guidare il mio spirito a tratti ribelle “nella feroce giungla” dell’Università.
- Ringrazio il **Dott. Alessandro Longo** ed il **Dott. Francesco Giannici** per aver contribuito a questo lavoro di ricerca. Ringrazio Alessandro anche per i suoi consigli professionali.
- Ringrazio **ESRF** (Grenoble) ed **ELETTRA** (Trieste) per il tempo-macchina concesso presso i rispettivi sincrotroni.
- Ringrazio il **Prof. Giulio Deganello** per avermi dato l’importante opportunità di lavorare presso lo **ISMN-CNR** di Palermo.
- Ringrazio la **Dott. Annamaria Venezia** per l’acquisizione e l’analisi dei dati XPS.
- Ringrazio **Francesco Giordano** per essere stato sempre disponibile ad un aiuto durante i giorni di lavoro presso lo ISMN-CNR di Palermo.
- Ringrazio la **Prof. Silvia Licoccia** per avermi dato l’importante opportunità di lavorare presso il **Dipartimento di Scienze e Tecnologie Chimiche dell’Università di Roma Tor Vergata**.

- Ringrazio la **Dott. Elisabetta Di Bartolomeo**, la **Dott. Alessandra D'Epifanio**, e **Chiara Pugnalini** per aver contribuito all'acquisizione dei dati di conducibilità, e le ringrazio per i loro consigli professionali.
- Ringrazio con affetto **Igor Luisetto** per essere stato sempre disponibile ad un aiuto durante i giorni di lavoro presso l'Università di Roma Tor Vergata… davvero un prezioso aiuto in "trasferta".
- Un grande ringraziamento anche al **Prof. Gilberto Vlaic** e al **Prof. Settimio Mobilio** per avermi dato l'importante opportunità di partecipare alla scuola internazionale **"X School on Synchrotron Radiation 2009"** ottimamente organizzata dalla **Società Italiana di Luce di Sincrotrone** e dal Sincrotrone **ELETTRA** (Duino, Settembre 2009).
- E grazie anche a **Veronica**.

Grazie.

CURRICULUM VITAE

Personal Informations

First name(s) / Surname(s): **Diego, Angelo Messana**

Photo:

Address(es): 38, via Torino, 90133, Palermo (PA), Italy
18, via Veneto, 93100, Caltanissetta (CL), Italy

Telephone(s): +393208840885; +393395879442

E-mail: Diego.messana.ded@gmail.com

Nationality: Italian

Date of birth: **20 May 1979**

Work experience

Dates: **2009-2010**
Occupation or position held: **Tutor in Chemistry at University**
Main activities: Teacher: basic chemistry course (OFA) and chemistry tutorials
Name of employer: Facoltà di Medicina e Chirurgia, Università degli Studi di Palermo (Italy)

Education and training

Dates: Started in **2008**
Title of qualification awarded: **Ph.D. in Chemistry**
Principal subjects: Project: "New proton conductors for electrochemical applications: synthesis and structure-properties correlation".
(in situ-XRD, EXAFS data personally collected at ESRF and ELETTRA Synchrotrons, EIS data personally collected at Università di Roma "Tor Vergata")
Supervisor: Prof. A. Martorana

Name and type of organisation providing education and training: Scuola di Dottorato di Ricerca in Scienze Chimiche, Università degli Studi di Palermo (Italy).

Dates: 23 July **2007**
Title of qualification awarded: **University Degree in Chemistry**
Principal subjects: Fields of study: Inorganic Chemistry, Physical Chemistry, Organic Chemistry, Analytical Chemistry, Material Science, Physics. Experimental Thesis: "Synthesis and structural analysis of metal nano-clusters". (XRD data personally collected at ESRF Synchrotron) Supervisor: Prof. A. Martorana

Name and type of organisation
providing education and training: Università degli Studi di Palermo (Italy)
Level in national or international classification: Grade: 107/110

Dates: **1997**
Title of qualification awarded: **High School License (Maturità Scientifica)**
Name and type of organisation
providing education and training: Liceo Scientifico Statale A. Volta, Caltanissetta (Italy)
Level in national or international classification: Grade: 60/60

Professional training

Dates: 07-18 September **2009**
Title of qualification awarded: **X School on Synchrotron Radiation**
Principal subjects: Synchrotron radiation techniques
Name and type of organisation
providing education and training: Società Italiana Luce di Sincrotrone, Synchrotron ELETTRA, Duino (Italy)
Organizers: Prof. G. Vlaic, S. Mobilio

Dates: 12-23 Settember **2005**
Title of qualification awarded: **9th Laboratory Course Neutron Scattering**
Principal subjects: Neutron Scattering techniques
Name and type of organisation
providing education and training: Forschungszentrum, Jülich (Germany)
Organizers: Prof. D. Ritchter, Dr. R. Zorn

Scientific Publications

"Crystal structure and local Dynamics in Tetrahedral Proton-Conducting $La_{1-x}Ba_{1+x}GaO_4$"
F. Giannici, D. Messana, A. Longo, and A. Martorana
Journal of Physical Chemistry C 115 **(2011)** 298-304

"Local structure of gallate proton conductors"
F. Giannici, D. Messana, A. Longo, L. Sciortino, and A. Martorana
Journal of Physics: Conference Series 190 **(2009)** 1-4

Conferences Partecipation

Conference: **Società Chimica Italiana Congresso Congiunto Sezioni Sicilia e Calabria**
2-3 December **2010**, Palermo (Italy)
Poster/Oral presentation: Poster: "Proton conduction and structure of $RE_{1-x}Ba_{1+x}GaO_{4-x/2}$ (RE = La,Nd)"
D. Messana, E. Di Bartolomeo, A. D'Epifanio, F. Giannici, S. Licoccia, A. Longo, and A. Martorana

Conference: **FIGIPAS 2009 Meeting in Inorganic Chemistry**
1-4 July **2009**, Palermo (Italy)
Poster/Oral presentation: Poster: "Synthesis and structural analysis of novel proton conductors $RE_{1-x}Ba_{1+x}GaO_{4-x/2}$ (RE = La,Nd)"
D. Messana, F. Giannici, A. Longo, and A. Martorana

Conference: **XVI SILS Meeting**
26-28 June **2008**, Palermo (Italy)
Poster/Oral presentation: Participation in Organizing Committee.
Poster: "Indium doping in proton-conducting oxides"
D. Messana, F. Giannici, A. Longo, A. Balerna, and A. Martorana

Languages

Native language: **Italian**

Foreign languages: **English**, Intermediate level (B1/B2)
French, Intermediate level (B1/B2)

Social skills and competences
- good social skills
- enthusiasm in multicultural environments
- great will power

Technical skills and competences
- Very good knowledge of techniques: **XRD** (X-ray Diffraction), **EXAFS** (Extended X-ray Absorption Fine Structure), **EIS** (Electrochemical Impedance Spectroscopy), **TGA** (Thermo-Gravimetric Analysis)

Computer skills and competences
- Very good knowledge of softwares: Microsoft Word, Microsoft Excel, Microsoft PowerPoint, Microsoft Paint, Windows Movie Maker, Microcal Origin, Kaleidagraoh, ChemSketch, ChemDraw, GSAS, VESTA, TA instruments-Universal Analysis, feff08, Viper, ZSimpWin
- Good knowledge of programming language Fortran90

Artistic skills and competences
Italian Literary prizes:
3th at "Premio Nazionale di Poesia Sabina Cavagliè, Dire" (1995)
2nd at "Premio Nazionale di Poesia Sabina Cavagliè, Dire" (1996)
Partetipation at "8th Premio Letterario Internazionale L'artigiano Poeta" (1999)

Driving licence
Driving licence BS

Additional Information
Chemist Qualification Test, 07 December 2007 at Università degli Studi di Palermo (Italy).
Experiments:
24-29 September 2009, experiment ma-669 at GILDA, **ESRF** Synchrotron (France)
04-10 February 2009, experiment ch-2714 at ID11, **ESRF** Synchrotron (France)
02-07 December 2008, experiment 2008027 at XAFS, **ELETTRA** Synchrotron (Italy)
19-24 June 2006, experiment hs-3084 at BM01, **ESRF** Synchrotron (France)